

# THE NEXT GENERATION VIRGO CLUSTER SURVEY. VI. THE KINEMATICS OF ULTRA-COMPACT DWARFS AND GLOBULAR CLUSTERS IN M87

HONG-XIN ZHANG<sup>1,2,3,4</sup>, ERIC, W. PENG<sup>1,2</sup>, PATRICK CÔTÉ<sup>5</sup>, CHENGZE LIU<sup>6,7</sup>, LAURA FERRARESE<sup>5</sup>, JEAN-CHARLES CUILLANDRE<sup>8</sup>, NELSON CALDWELL<sup>9</sup>, STEPHEN D. J. GWYN<sup>5</sup>, ANDRÉS JORDÁN<sup>10</sup>, ARIANE LANÇON<sup>11</sup>, BIAO LI<sup>1,2</sup>, ROBERTO P. MUÑOZ<sup>10,11</sup>, THOMAS H. PUZIA<sup>10</sup>, KENJI BEKKI<sup>12</sup>, JOHN BLAKESLEE<sup>5</sup>, ALESSANDRO BOSELLI<sup>13</sup>, MICHAEL J. DRINKWATER<sup>14</sup>, PIERRE-ALAIN DUC<sup>15</sup>, PATRICK DURRELL<sup>16</sup>, ERIC EMSELLEM<sup>17,18</sup>, PETER FIRTH<sup>14</sup>, RUBEN SÁNCHEZ-JANSSEN<sup>5</sup>

<sup>1</sup>Department of Astronomy, Peking University, Beijing 100871, China; hongxin@pku.edu.cn; peng@pku.edu.cn

<sup>2</sup>Kavli Institute for Astronomy and Astrophysics, Peking University, Beijing 100871, China

<sup>3</sup>CAS-CONICYT Fellow

<sup>4</sup>Chinese Academy of Sciences South America Center for Astronomy, Camino El Observatorio #1515, Las Condes, Santiago, Chile

<sup>5</sup>National Research Council of Canada, Herzberg Astronomy and Astrophysics Program, 5071 West Saanich Road, Victoria, BC V9E 2E7, Canada

<sup>6</sup>Center for Astronomy and Astrophysics, Department of Physics and Astronomy, Shanghai Jiao Tong University, Shanghai 200240, China

<sup>7</sup>Shanghai Key Lab for Particle Physics and Cosmology, Shanghai Jiao Tong University, Shanghai 200240, China

<sup>8</sup>Canada–France–Hawaii Telescope Corporation, Kamuela, HI 96743, USA

<sup>9</sup>Harvard-Smithsonian Center for Astrophysics, Cambridge, MA, 02138

<sup>10</sup>Instituto de Astrofísica, Facultad de Física, Pontificia Universidad Católica de Chile, Av. Vicuña Mackenna 4860, 7820436 Macul, Santiago, Chile

<sup>11</sup>Observatoire astronomique de Strasbourg, Université de Strasbourg, CNRS, UMR 7550, 11 rue de l'Université, F-67000 Strasbourg, France

<sup>12</sup>School of Physics, University of New South Wales, Sydney 2052, NSW, Australia

<sup>13</sup>Aix Marseille Université, CNRS, LAM (Laboratoire d'Astrophysique de Marseille) UMR 7326, F-13388 Marseille, France

<sup>14</sup>School of Mathematics and Physics, University of Queensland, Brisbane, QLD 4072, Australia

<sup>15</sup>Laboratoire AIM Paris-Saclay, CNRS/INSU, Université Paris Diderot, CEA/IRFU/SAP, F-91191 Gif-sur-Yvette Cedex, France

<sup>16</sup>Department of Physics & Astronomy, Youngstown State University, Youngstown, OH 44555

<sup>17</sup>Université de Lyon 1, CRAL, Observatoire de Lyon, 9 av. Charles André, F-69230 Saint-Genis Laval; CNRS, UMR 5574; ENS de Lyon, France

<sup>18</sup>European Southern Observatory, Karl-Schwarzschild-Str. 2, D-85748 Garching, Germany

*To appear in The Astrophysical Journal*

## ABSTRACT

We present the dynamical properties of 97 spectroscopically confirmed ultra-compact dwarfs (UCDs;  $r_h \gtrsim 10$  pc) and 911 globular clusters (GCs) associated with central cD galaxy of the Virgo cluster, M87. Our UCDs, of which 89% have  $M_\star \gtrsim 2 \times 10^6 M_\odot$  and 92% are as blue as the classic blue GCs, nearly triple previously confirmed sample of Virgo UCDs, providing by far the best opportunity for studying global dynamics of UCDs. We found that (1) UCDs have a surface number density profile that is shallower than that of blue GCs in the inner  $\sim 70$  kpc and as steep as that of red GCs at larger radii; (2) UCDs exhibit a significantly stronger rotation than GCs, and blue GCs seem to have a velocity field that is more consistent with that of the surrounding dwarf ellipticals than with that of UCDs; (3) UCDs have an orbital anisotropy profile that is tangentially-biased at radii  $\lesssim 40$  kpc and radially-biased further out, whereas blue GCs become more tangentially-biased at larger radii beyond  $\sim 40$  kpc; (4) GCs with  $M_\star \gtrsim 2 \times 10^6 M_\odot$  have rotational properties indistinguishable from the less massive ones, suggesting that it is the size, instead of mass, that differentiates UCDs from GCs as kinematically distinct populations. We conclude that most UCDs in M87 are not consistent with being merely the most luminous and extended examples of otherwise normal GCs. The radially-biased orbital structure of UCDs at large radii is in general agreement with the “tidally threshed dwarf galaxy” scenario.

*Subject headings:* galaxies: clusters: individual (Virgo, M87/NGC4486) – galaxies: star clusters: general – globular clusters: general – galaxies: nuclei – galaxies: elliptical and lenticular, cD – galaxies: kinematics and dynamics

## 1. INTRODUCTION

Ultra-compact dwarfs (UCDs; Philipps et al. 2001) were originally discovered (Hilker et al. 1999b; Drinkwater et al. 2000a) as compact stellar systems which are more than 1 mag brighter than the known brightest globular clusters ( $M_V \sim -11$  mag; Harris 1991) but at least 2 mag fainter than the prototypical compact elliptical M32 ( $M_V = -16.4$  mag). The first five UCDs found in the core of the Fornax Cluster were unresolved or marginally resolved on ground-based arcsec-resolution images, implying effective radii of  $r_h \lesssim 100$  pc. Subsequent *Hubble*

*Space Telescope* (HST) imaging of those Fornax UCDs (Drinkwater et al. 2004) gave  $r_h \gtrsim 10$  pc, which differs significantly from  $r_h$  of  $\sim 3$  pc for conventional GCs (e.g. van den Bergh et al. 1991; Jordán et al. 2005). Since their discovery in the Fornax Cluster, similarly bright UCDs have been found in other clusters (Virgo: Hasegan et al. 2005; Jones et al. 2006; Abell S0740: Blakeslee & Barber DeGraaff 2008; Coma: Madrid et al. 2010; Chiboucas et al. 2011; Centaurus: Mieske et al. 2009; Hydra: Misgeld et al. 2011; Antlia: Caso et al. 2013), groups (HCG22 and HCG90: Da Rocha et al. 2011; NGC1132: Madrid

& Donzelli 2013), and even relatively isolated galaxies (Sombrero: Hau et al. 2009; NGC 4546: Norris & Kannappan 2011).

Given the intermediate nature of UCDs, since their discovery, there has been ongoing debate about their origin. The few proposed formation mechanisms in the literature are: (1) they are merely luminous, genuine GCs (Murray 2009), or mergers of young massive star clusters formed in starburst regions, such as those formed during collisions between gas-rich galaxies (Fellhauer & Kroupa 2002; Bruns et al. 2011; Renaud, Bournaud & Duc 2014); (2) they are the remains of tidally-stripped nucleated galaxies (e.g. Bekki et al. 2003; Goerdt et al. 2008; Pfeffer & Baumgardt 2013); (3) they are the remnants of primordial compact galaxies (Drinkwater et al. 2004).

A consensus about the primary origin of UCDs has yet to be reached. In fact, even the name given to this category of object, ultra-compact dwarf, has been debated. Since the UCD designation implies a galactic origin, they have also been referred to as “dwarf-globular transition objects” (DGTOs, Hasegan et al. 2005). In this paper, we will refer to these objects as UCDs since that is the most common usage in the literature, but our usage is not meant to pre-suppose their origin.

The three properties of UCDs that make them distinct from GCs include their larger sizes (e.g. Kissler-Patig, Jordán & Bastian 2006), a possible size-luminosity relation (e.g. Côté et al. 2006; Dabringhausen et al. 2008) and slightly elevated dynamical mass-to-light ratios (e.g. Hasegan et al. 2005; Mieske et al. 2008) above a dynamical mass of  $\sim 2 \times 10^6 M_\odot$ . Mieske, Hilker & Mergeld (2012) found that the number counts of UCDs, which they defined as stellar systems with  $M_V < -10.25$ , in several different environments (the Fornax cluster, Hydra cluster, Centaurus cluster and the Local Group) are fully consistent with them being the bright tail of the normal GC population. On the other hand, Côté et al. (2006) and Brodie et al. (2011) found that UCDs follow dE nuclei, instead of GCs, on the color-magnitude diagram, suggesting that most UCDs may be a distinct population that is more likely to be related to tidally stripped galaxy nuclei, rather than to GCs.

Recently, Seth et al. (2014) found strong evidence for the existence of a supermassive black hole ( $2.1 \times 10^7$ ) in the brightest known UCD – M60-UCD1 ( $M_V = -14.2$  mag, Strader et al. 2013), indicating that this UCD is most probably a tidally stripped nucleus of a low-mass elliptical galaxy. Nevertheless, a spatially resolved analysis of the kinematics of the most luminous UCD in the Fornax cluster (UCD3,  $M_V = -13.6$  mag; Hilker et al. 1999) by Frank et al. (2011) found that its internal kinematics are fully consistent with it being merely a massive star cluster, without strong evidence for the presence of either an extended dark matter halo or a central black hole. Moreover, there exists direct evidence that UCD-like objects can form as supermassive star clusters, such as W3 in the merger remnant NGC 7252 ( $M_\star \sim 7 \times 10^7 M_\odot$ , age  $\sim$  a few 100 Myr: Maraston et al. 2004) and the recently discovered young “UCDs” (Penny et al. 2014) associated with star-forming regions in NGC 1275 (a member of the Perseus cluster).

All previous investigations of UCDs were based on ei-

ther incomplete or inhomogeneous small samples, which hinders us from understanding the global properties of UCDs in any one galaxy or environment. Over the past 5 years, we have been collecting low-resolution ( $R \sim 1300$ ) spectroscopic data for UCDs and luminous GCs toward the central regions of the Virgo cluster, using two multi-fiber spectrographs: the 2dF/AAOmega (Sharp et al. 2006) on the 3.9-m Anglo-Australian Telescope (AAT) and Hectospec (Fabricant et al. 2005) on the 6.5-m MMT. Our spectroscopic surveys of the Virgo UCDs and GCs have been highly efficient (in terms of contamination level of non-Virgo targets), thanks to an unprecedentedly clean sample of Virgo UCD and GC candidates selected based on the recently completed Next Generation Virgo Survey (NGVS, Ferrarese et al. 2012), which offers deep ( $g_{\text{limit}} = 25.9$  mag at  $10\sigma$  for point sources) and high resolution (FWHM  $\sim 0.6''$  in  $i$  band)  $u^*giz$  (and  $r$  in the cluster core) imaging data of the Virgo cluster from its core to the virial radius ( $\sim 104 \text{ deg}^2$ ) with the MegaCam instrument on the Canada-France-Hawaii Telescope.

Details of the spectroscopic surveys will be presented in future papers in a series. In this paper, we present a dynamical analysis of the UCDs associated with the central cD galaxy M87 ( $D = 16.5$  Mpc; Mei et al. 2007; Blakeslee et al. 2009), which hosts the majority of confirmed UCDs from our spectroscopic surveys, and thus provides the best opportunity for studying the dynamics and photometric properties of UCDs as a population. For comparison purposes, we also collected radial velocities of 911 GCs associated with M87, and did the dynamical analysis in parallel with the UCDs. Other papers in the NGVS series relevant to the topics covered here include a systematic study of photometrically-selected UCDs in the three Virgo giant ellipticals M87, M49 and M60 (Liu et al. 2015), studies of the distributions of cluster-wide GC populations in the Virgo cluster (Durrell et al. 2014), a detailed study of the spatial, luminosity and color distributions of GCs selected based on various NGVS bands in the central  $2^\circ \times 2^\circ$  around M87 (Lancon et al. in preparation), dynamical modeling of M87 GCs (Zhu et al. 2014), and the physical classification of stellar and galactic sources based on the optical and deep  $K_s$  imaging (Muñoz et al. 2014). Liu et al. (2015) is especially complementary to this work, in that it presents a thorough description of the photometry and size measurements of the UCD samples, and a detailed analysis of the color-magnitude relation, color distribution, specific frequencies, and spatial distribution of the UCDs.

This paper is structured as follows. In Section 2, we introduce the data and samples used in this work. A brief description of the methodology used to select a highly clean sample of Virgo UCDs and GCs from the spectroscopic catalogs is given in Section 3. The definition of our working subsamples is described in Section 4. Section 5 provides an overview of the UCD sample, including the spatial distribution, completeness and surface number density profiles. Section 6 presents the phase-space distribution and velocity dispersion profiles of the UCDs and GCs. Section 7 presents the velocity distributions of our samples. A kinematic modeling of the rotational properties of UCDs and GCs is given in Section 8, while Section 9 is devoted to a Jeans analysis for determining

the radial anisotropies of UCDs and GCs. A brief discussion and summary of this paper follow in Section 10.

## 2. DATA

This paper is devoted to a detailed dynamical analysis of confirmed UCDs ( $r_h \gtrsim 10$  pc) associated with the cD galaxy M87. To this end, we compiled a sample of spectroscopically confirmed UCDs, together with GCs which will be used for comparison purpose, from three different sources, i.e. our recently finished 2dF/AAOmega AAT and Hectospec/MMT surveys, and the radial velocity catalogs of Virgo GCs and UCDs compiled by Strader et al. (2011, hereafter S11). For duplicate observations among the three sources, a weighted average of the individual radial velocities will be used in this work. The location of the pointings around M87 covered by our AAT (*blue dotted circles*) and MMT (*small red dotted circles*) surveys is shown in Figure 1. It can be seen that our surveys covered most of the area encompassed by one scale radius (*big solid circle*) of the NFW dark matter halo toward the Virgo A subcluster (McLaughlin 1999).

The photometric data for the spectroscopic samples are from the NGVS. The reader is referred to Ferrarese et al. (2012) for a detailed description of the NGVS. Here we only mention that the average seeing of the NGVS *g*- and *i*-band imaging data in the central 4 square degrees around M87 is  $\sim 0.7''$  and  $0.6''$ , which makes it possible to measure (through profile modeling) the size of Virgo objects down to  $r_h$  of  $\gtrsim 5$  pc. The reader is referred to Liu et al. (2015, in preparation) for details about size measurements on NGVS images. In addition, we have obtained deep  $K_s$ -band imaging data for this region (NGVS-IR; Muñoz et al. 2014). Combining the  $K_s$  band with the NGVS optical band photometry allows us to identify most of the foreground stars which would otherwise contaminate our spectroscopic catalogs of Virgo UCDs and GCs.

All the magnitudes (in the MegaCam  $u^*griz$  filters) that appear in this paper are on the AB system. In addition, a subscript of 0 denotes the magnitude in question has been corrected for the Galactic extinction. In the remainder of this section, we give a brief introduction to the three individual radial velocity catalogs of Virgo UCDs and GCs. In addition, we will also introduce the radial velocity catalog of early-type dwarf galaxies surrounding M87. In this work, the velocity field of surrounding early-type dwarf galaxies will be compared to that of the UCDs and GCs.

### 2.1. The AAT sample

We have carried out (Mar 28 to Apr 1 in 2012) a systematic spectroscopic survey of compact stellar systems (GCs and UCDs) toward the central regions of the Virgo cluster (Virgo A subcluster), using the 2dF/AAOmega multi-fiber spectrograph on the 3.9-m Anglo-Australian Telescope (AAT). The survey consists of nine 2dF pointings, covering a total sky area of  $\sim 30$  deg<sup>2</sup>. The 8 pointings around M87 are shown as *blue dotted circles* in Figure 1. The observations cover a wavelength range from  $\sim 3700$  Å to  $8800$  Å, with a resolution of  $R = 1300$ .

The candidates for our survey were selected to fall in the region occupied by spectroscopically confirmed Virgo GCs and UCDs on the MegaCam  $u^* - g$  vs.  $g - i$  dia-

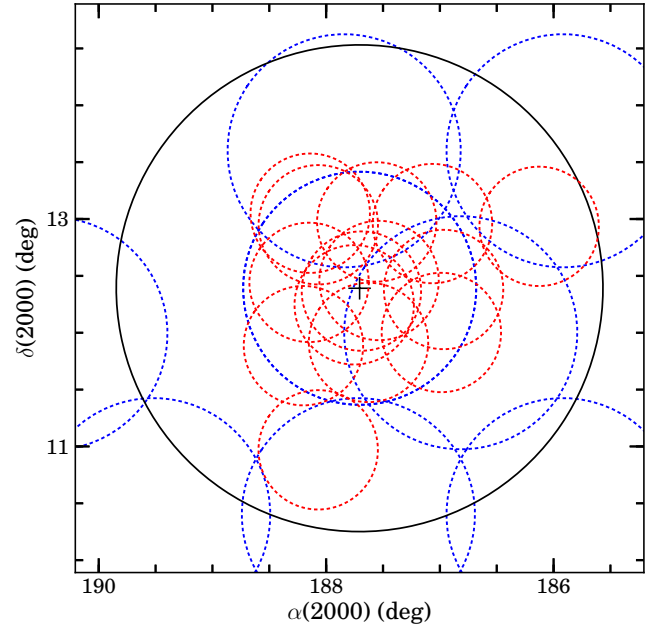


FIG. 1.— Location of the fields covered by our AAT (*blue dotted circles*,  $1^\circ$  in radius each) and MMT (*small red dotted circles*,  $0.5^\circ$  in radius each) surveys. The *big black solid circle* marks the scale radius ( $2.143 = 0.617$  Mpc) of the NFW model fitted to the surrounding dark matter halo of the Virgo A subcluster (McLaughlin 1999). The *black plus* marks the photometric center of M87.

gram\*, and have  $18.5 \leq g \leq 20.5$  magnitude ( $-12.6 \leq M_g \leq -10.6$  at a distance of 16.5 Mpc for the Virgo cluster). The Virgo UCD candidates were mainly selected to have  $10 \lesssim r_{h,NGVS} \lesssim 30$  pc, and the GC candidates have  $1 < r_{h,NGVS} < 10$  pc, where  $r_{h,NGVS}$  is the half-light radius (assuming a distance of the Virgo cluster) measured based on the NGVS *g* and *i* images.

The AAT survey obtained radial velocities of 55 Virgo UCDs and 52 GCs, of which 22 UCDs and 20 GCs have no published velocities before. At the limiting magnitude of  $g \sim 20.5$ , we obtained radial velocities with errors of  $\sim 30$  km s<sup>-1</sup> in a typical exposure time of 1.5 hour.

### 2.2. The MMT sample

In 2009 and 2010, we used the Hectospec multifiber spectrograph (Fabricant et al. 2005) on the 6.5-meter MMT telescope to carry out an extensive spectroscopic survey ( $3650\text{--}9200\text{Å}$ ,  $R = 1000$ ) of the central  $2^\circ \times 2^\circ$  ( $576 \times 576$  kpc) around M87 in three observing runs. The MMT pointings around M87 are shown as *small red dotted circles* in Figure 1.

Similar to the AAT survey, the GC and UCD candidates for this survey were selected using MegaCam  $u^*giz$  photometry from NGVS imaging. At the limiting magnitude ( $g < 22.5$ ) of this survey, we obtained radial velocities with errors of  $\sim 30$  km s<sup>-1</sup> in two hour exposures. This survey produced radial velocities for 324 GCs and 51 UCDs, of which 207 GCs and 18 UCDs (excluding the ones discovered by our AAT survey) have no published velocities before.

\* By the time we prepared input catalogs for our spectroscopic surveys (including the MMT survey described below), the NGVS-IR  $K_s$  band data, which is very efficient in separating out the foreground stars, was not available.

### 2.3. The S11 sample

By combining radial velocities from the literature (Huchra & Brodie 1987; Mould et al. 1990; Cohen 2000; Hanes et al. 2001; Jones et al. 2006; Hasegan et al. 2007; Evstigneeva et al. 2007; Firth et al. 2009; Paudel et al. 2010) and from their new observations, S11 compiled a sample of 927 radial velocities toward the central  $\sim 40'$  of M87. Of these, 737 were classified as Virgo GCs and UCDs. Given the high-quality multi-band imaging data from the NGVS, we re-classified (Section 3) the original 927 objects from S11, and found another 5 low-velocity objects belonging to the Virgo cluster.

### 2.4. Early-type Dwarf Galaxies Surrounding M87

Our surveys extend to the Virgo intra-cluster region. We will compare the kinematics of UCDs and GCs in the outermost part of M87 to the surrounding early-type dwarf galaxies, in order to explore any possible connection. Within a geometric radius of  $2^\circ$  from M87, there are 326 galaxies (either with radial velocity unavailable or  $< 3500 \text{ km s}^{-1}$ ) classified as either dE or dS0 galaxies in the Virgo Cluster Catalog (VCC, Binggeli & Cameron 1991). Among the 326 galaxies, 67 were further classified as nucleated dE galaxies (dE, N)<sup>†</sup>. 59 of the 67 dE,N galaxies and 67 of the non-nucleated dE/dS0 galaxies have radial velocities available in the literature, as compiled by the GOLDMine project (Gavazzi et al. 2003). In addition, our AAT and MMT surveys obtained the first radial velocity measurements for another 2 dE galaxies, i.e. VCC1317 ( $V = 327 \pm 39 \text{ km s}^{-1}$ ) and VCC1244 ( $V = 824 \pm 33 \text{ km s}^{-1}$ ). In this work, we will be comparing the velocity field (number density profiles) of the 128 (326) galaxies with that of the M87 UCDs and GCs.

## 3. IDENTIFICATION OF VIRGO OBJECTS

### 3.1. Culling Out the Virgo Objects

There exists contamination from both background galaxies and foreground stars in our spectroscopic catalogs. There is a well-defined gap between the Virgo galaxies and background galaxies at radial velocities  $\sim 3000 \text{ km s}^{-1}$ , so a simple cut in radial velocity at  $3000 \text{ km s}^{-1}$  can remove all background galaxies. At the low-velocity end ( $V_{\text{los}} < 400 \text{ km s}^{-1}$ ), to cull foreground stars from the spectroscopic catalogs, we made use of the  $u^* - i$  vs.  $i - K_s$  color-color diagram, which has been shown to clearly separate nearly all foreground stars (Muñoz et al. 2014) from Virgo stellar systems (with the exception of some metal-poor G-type stars). For sources that fall inside the overlap area of the bona-fide Virgo members and foreground stars on the  $u^* - i$  vs.  $i - K_s$  diagram (see Muñoz et al. 2014), we further require that the sources should have half-light radii  $r_h$  measured (on the NGVS  $g$ - and  $i$ -band images) to be  $> 0.06''$ , corresponding to a linear scale of  $\sim 5 \text{ pc}$  at the distance of Virgo cluster. The high-quality NGVS  $g$  and (especially)  $i$  imaging data can resolve Virgo sources down to  $r_h \sim 5 - 10 \text{ pc}$ .

The half-light radius  $r_{h,\text{NGVS}}$  of each source was derived as a weighted average of two independent measurements in the  $g$  and  $i$  bands by fitting PSF-convolved King

<sup>†</sup> One should keep in mind that the real fraction of dE, N galaxies is most probably much higher than 21% (67/326), as demonstrated by Côté et al. (2006) based on high-quality HST imaging data of 100 early-type galaxies in the Virgo cluster.

(1966) models to NGVS images with the KINGPHOT software package (Jordán et al. 2005). Briefly, when using KINGPHOT, we adopted a fixed concentration parameter  $c$  of 1.5 and a fixed fitting radius  $r_{\text{fit}}$  of  $1.3''$  ( $\simeq 105 \text{ pc}$  at the Virgo distance). According to Jordán et al. (2005), the KINGPHOT size measurement suffers from large biases when  $r_h \gtrsim r_{\text{fit}}/2$ , which is however not expected to be a problem for our analysis because all but one (VUCD7) of previously confirmed Virgo UCDs have  $r_h < 50 \text{ pc}$ .

### 3.2. Separating the Virgo UCDs from GCs

A UCD is defined to have  $10 \lesssim r_h \lesssim 100 \text{ pc}$  in this work (see Section 4). At  $10 \lesssim r_h \lesssim 20 \text{ pc}$ , the Virgo UCDs are only marginally resolved in the NGVS images. Assuming a Gaussian-shaped PSF, the typical FWHM of the NGVS  $i$ -band seeing disc ( $0.6''$ ) is equivalent to an  $r_h$  of  $0.172''$ , which corresponds to  $\sim 14 \text{ pc}$  at the distance of the Virgo cluster. Therefore, size measurements based on the NGVS images are especially sensitive to the S/N and possible inaccuracy of the PSF, and are unavoidably subject to relatively large uncertainties compared to the measurements based on HST images. Our test with the NGVS images suggests that, sources with  $g \gtrsim 21.5 - 22 \text{ mag}$  are subject to relatively large bias and uncertainties ( $> 20\%$ ) in their size measurement, and thus are not suitable for our analysis. To pick out a clean sample of UCDs based on NGVS images, we require UCDs to have  $r_{h,\text{NGVS}} \geq 11 \text{ pc}$ ,  $\Delta r_{h,\text{NGVS}}/r_{h,\text{NGVS}} < 0.1$ , and  $g \leq 21.5$  ( $M_g \leq -9.6$ ). In addition, sources with  $r_{h,\text{HST}} > 9.5 \text{ pc}$  based on measurements with existing HST images (e.g. S11; Jordán et al. 2005) are also included as UCDs, regardless of their brightness. All the other confirmed Virgo compact clusters are regarded to be GCs.

By comparing our size measurements with that determined with existing HST imaging data (see Table 5), our size criteria of UCD selection based on the NGVS measurements result in zero contamination from Virgo objects with  $r_{h,\text{HST}} < 10 \text{ pc}$ . Among the old sample of 34 Virgo UCDs with  $r_{h,\text{HST}} > 9.5 \text{ pc}$ , 3 did not have NGVS size measurements due to their proximity (within  $10''$ ) to saturated foreground stars, 28 have  $r_{h,\text{NGVS}} \geq 11 \text{ pc}$ , 1 (T15886:  $g = 22.97 \text{ mag}$ ) has  $10 \leq r_{h,\text{NGVS}} < 11 \text{ pc}$ , and the other 2 (S6004:  $g = 21.32$ ; S8006:  $g = 20.53$ ) have  $r_h$  measured to be less than  $10 \text{ pc}$  either in NGVS  $g$  or  $i$  band. Therefore, by selecting UCD-sized objects ( $r_h \gtrsim 10 \text{ pc}$ ) based on the NGVS images, we may miss  $\sim 6\%$  of genuine UCDs at  $g < 21.5 \text{ mag}$  and  $\lesssim 3\%$  at  $g < 20.5 \text{ mag}$ .

### 3.3. The Samples of UCDs and GCs

Given the above selection procedure, we end up with a total number of 97 UCDs and 911 GCs, which fall within  $1.5^\circ$  of M87 and are not associated with any galaxies other than M87 based on spatial location and radial velocities. Some of these UCDs and GCs, especially those at the outermost radii, probably belong to the intra-cluster population. The full sample of UCDs is listed in Table 5. The sample of GCs has been recently used by Zhu et al. (2014) to determine the dynamical mass profile of M87. The full catalog of GCs will be presented elsewhere (Peng et al. 2015, in preparation). The 34 UCDs confirmed previously in the literature (old sample, Brodie et

al. 2011) and the 63 newly confirmed UCDs (new sample) are listed separately in Table 5. For Virgo objects that were already spectroscopically confirmed (as compiled by S11), we follow the old naming; for the newly confirmed Virgo members, we adopted a naming scheme which starts with “M87UCD-”. Note that, the column  $r_{h,NGVS}$  gives the weighted average half-light radius measurements in the NGVS  $g$  and  $i$  bands. The  $r_{h,HST}$  measurement (Jordán et al. 2005; Jordán et al. 2009; S11), if available, is also listed. We point out that the uncertainties of  $r_{h,NGVS}$  reported in Table 5 only include the formal errors returned from the KINGPHOT fitting, and do not take into account any potential systemic uncertainty, such as the degree of accuracy of the PSF and suitability of King models for representing the UCD light profiles.

Our sample of UCDs is nearly 3 times larger than previously known (34) Virgo UCDs, and our GC sample is  $\sim 20\%$  larger than that of S11. Radial velocities for 39 of the 97 UCDs were obtained from our AAT and MMT surveys for the first time. In terms of spatial coverage, one of the most important improvement of our GC sample is at the projected galactocentric distances larger than  $30'$  from M87. Specifically, our sample includes 63 GCs in the projected radius range from  $30'$  to  $60'$ , and this is 7 times larger than that of S11. While the full catalog of M87 GCs will be presented elsewhere, we emphasize that the main results related to GCs in this paper would not change qualitatively if only the S11 sample of GCs was used in our analysis because of the already large spectroscopic sample of M87 GCs in the literature. Since the surface number density of UCDs is relatively low, our kinematic analysis will be carried out in a coarser spatial (or radial) resolution than previous studies (Côté et al. 2001; S11). Therefore, whenever relevant, we refer the readers to Côté et al. (2001) and S11 for a more detailed kinematical analysis of M87 GCs within the central  $30'$ .

#### 4. DEFINITION OF WORKING SAMPLES

The primary goal of this work is to explore the differences or similarities between UCDs and GCs. To this end, we define the following subsamples in this paper.

- **UCDs.** UCDs are distinguished from GCs as having half-light radius  $r_h \gtrsim 10$  pc (although in practice we require  $r_{h,NGVS} \geq 11$  pc, as described above) in this work. The two most commonly adopted definitions of UCDs are mass ( $2 \times 10^6 \lesssim M_{\text{dyn}} \lesssim 10^8 M_\odot$ ; e.g. Hasegan et al. 2005; Mieske et al. 2008) and/or  $r_h$  ( $10 \lesssim r_h \lesssim 100$  pc; e.g. Norris et al. 2011; Brodie et al. 2011). The mass definition is justified by the findings that 1) compact stellar systems with  $M \gtrsim 2 \times 10^6$  tend to have  $M/L$  significantly higher than the lower mass systems; 2) there seems to be a size-luminosity relation setting in at  $M \gtrsim 2 \times 10^6$  (e.g. Rejkuba et al. 2007; Evstigneeva et al. 2008; Dabringhausen et al. 2008; Norris & Kannappan 2011), in contrast to the more or less constant  $r_h$  ( $\sim 3$  pc, e.g. van den Bergh et al. 1991; Jordán et al. 2005) of “normal” GCs. The size definition of UCDs differentiates them from normal GCs as dynamically un-relaxed stellar systems (e.g. Mieske et al. 2008). The two definitions may converge at the highest mass end. While we adopted the size definition in this work, we will try

to explore the significance of mass in differentiating UCDs as stellar systems distinct from normal GCs.

- **Blue GCs and Red GCs.** A double-Gaussian fitting to the NGVS  $(g-i)_0$  bimodal color distribution of photometrically-selected GCs in M87 suggests that the blue and red components cross at  $(g-i)_0 = 0.89$  mag. Therefore, we classified GCs as blue ( $N=683$ ) and red ( $N=228$ ) at a dividing  $(g-i)_0 = 0.89$  mag.
- **Bright GCs and faint GCs.** Bright GCs and faint GCs are separated at NGVS  $i_0 = 20.5$  magnitude, which corresponds to a stellar mass of  $\sim 1.6 - 2 \times 10^6 M_\odot$  at  $[\text{Fe}/\text{H}]$  ranging from  $-1.3$  (the typical value for blue GCs in M87; Peng et al. 2006) to  $-0.3$  (the typical value for red GCs in M87) for a 10 Gyr old stellar population with a Chabrier or Kroupa stellar initial mass function (IMF). The dividing magnitude (or mass) was chosen to roughly correspond to the proposed mass boundary between UCDs and GCs for the mass definition of UCDs. By separating the bright GCs from the faint GCs, we will explore the importance of mass or luminosity in differentiating UCDs from GCs.

The median  $(g-i)_0$  of our samples of UCDs and blue GCs are 0.75 and 0.74 respectively, and about 92% of our UCDs fall into the color range of the blue GCs. So we will place additional emphasis on a comparison between dynamical properties of UCDs and blue GCs throughout this paper.

### 5. OVERVIEW OF THE UCD AND GC SAMPLES

#### 5.1. 2D Spatial Distribution

Figure 2 presents the spatial distributions of all spectroscopically confirmed UCDs, GCs and dE galaxies around M87. Data from our AAT survey, MMT survey, and S11 are represented by different colors. Different types of objects are plotted as different symbols. When plotting Figure 2, for duplicated observations among the three data sources, we group them into, in order of priority, the S11 catalog, the AAT survey catalog, and the MMT survey catalog. Figure 3 shows the spatial distribution of UCDs, color-coded according to their line-of-sight velocities.

Like the GC system (e.g. McLaughlin et al. 1994; Forte et al. 2012; Durrell et al. 2014), the spatial distribution of the UCDs broadly follows the stellar diffuse light. Within  $2^\circ$  of M87, the outermost confirmed UCD has a projected galactocentric distance  $R_p$  of  $55'$  from the center of M87, the outermost red and blue GCs have  $R_p = 49'$  and  $85'$  respectively, with only one GC lying within  $65' < R_p < 85'$ .

An interesting “overdensity” of  $\sim 11$  UCDs can be seen toward the northwest of M87 between  $\sim 15'$  and  $30'$ . After checking the radial velocity distribution of UCDs belonging to this spatial “overdensity”, we found that the “members” of this overdensity have radial velocities ranging from  $\sim 900$  to  $1750 \text{ km s}^{-1}$ , suggesting this “overdensity” is due to chance alignment, rather than a physical substructure.

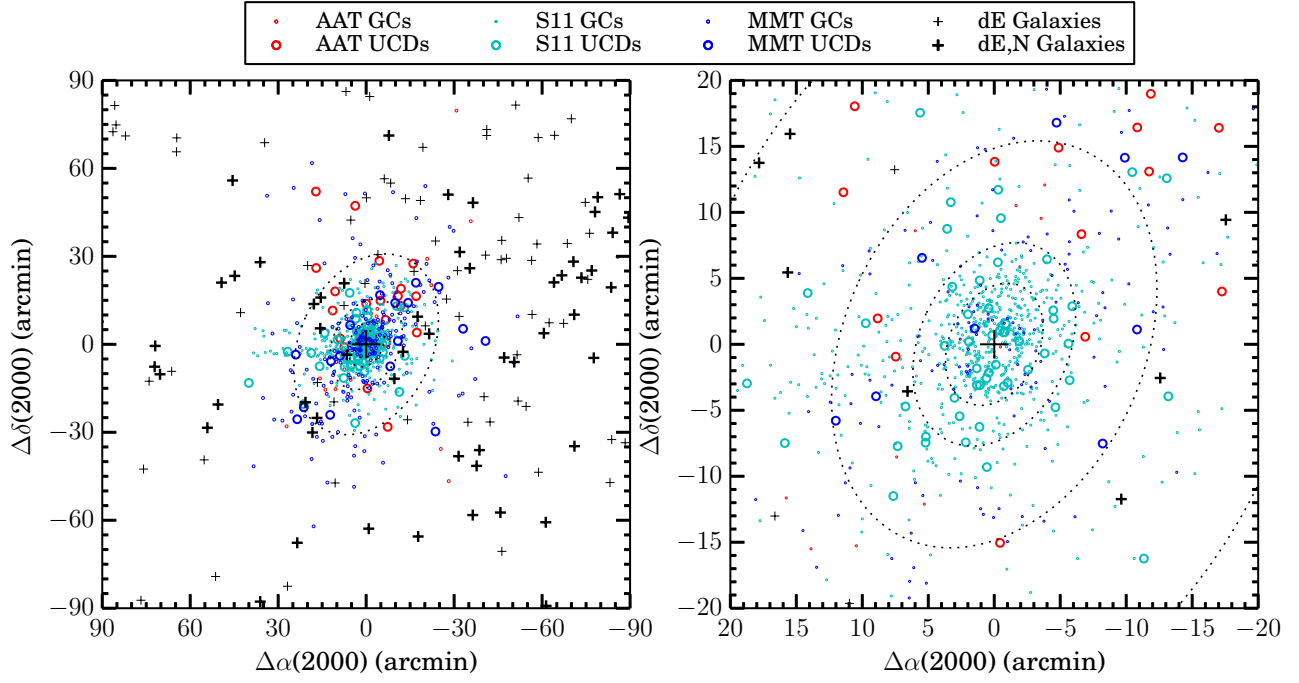


FIG. 2.— Spatial distribution of spectroscopically confirmed GCs, UCDs, and dE galaxies within the central  $1.5^\circ$  (left panel) and the central  $20'$  (right panel) of M87. Dotted ellipses represent the stellar isophotes of M87 at  $3R_e$ ,  $5R_e$ ,  $10R_e$  and  $20R_e$ , where  $R_e$  is the effective radius measured based on the NGVS  $g$ -band image. Different colors indicate data sets from different sources. The large black plus marks the photometric center of M87.

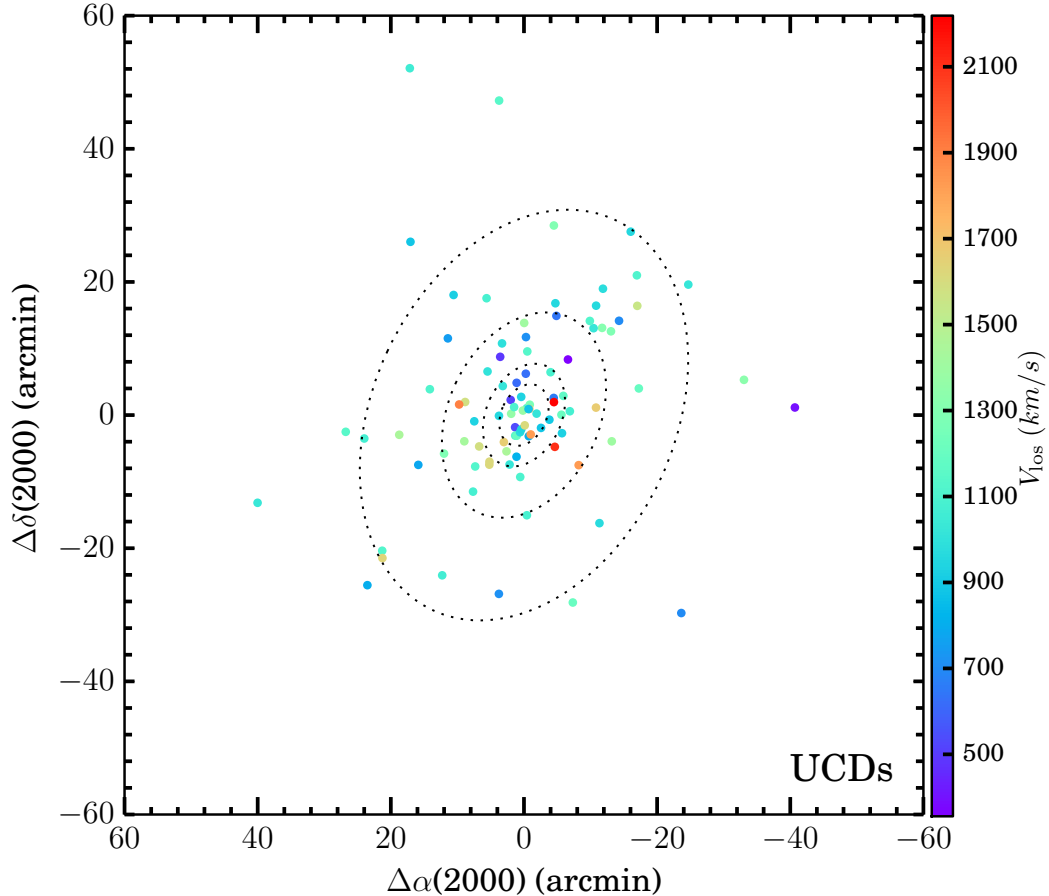


FIG. 3.— Spatial distribution of spectroscopically confirmed UCDs around M87. As in Figure 2, dotted ellipses represent the stellar isophotes of M87 at  $3R_e$ ,  $5R_e$ ,  $10R_e$  and  $20R_e$ . The plotted objects are color-coded based on their line-of-sight velocities.



In what follows, we will be mostly working with the geometric average radius  $R_{\text{av}}$  when exploring various radial trends.  $R_{\text{av}}$  is defined to be equal to  $a\sqrt{1-\epsilon}$ , where  $a$  is the length along the semi-major axis ( $\text{PA} \simeq 155^\circ$ ) and  $\epsilon$  is the ellipticity. Given that the spatial distribution of UCDs and GCs, in terms of flattening and orientation, roughly matches the stellar diffuse light of M87 (Durrell et al. 2014), we adopted the radial profiles of  $\epsilon$  and PA of the stellar isophotes of M87 determined with the high-quality NGVS  $g$ -band imaging data. Our measurements of  $\epsilon$ , ranging from  $\sim 0$  in the central  $0.5'$  to  $0.33$  around  $10' - 15'$  along the semi-major axis, are in good agreement with previous studies (e.g. Ferrarese et al. 2006; Kormendy et al. 2009). Measurements of  $\epsilon$  beyond  $\sim 15'$  are subject to relatively large uncertainties, so we fixed  $\epsilon$  as  $0.33$  at  $a > 15'$ .

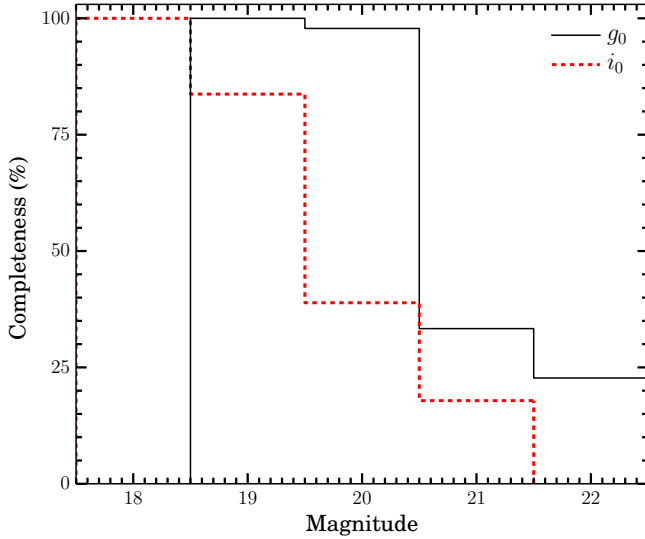


FIG. 4.— Completeness levels of our sample of UCDs as a function of magnitude in  $g$  (black solid lines) and  $i$  (red dotted lines) bands.

### 5.2. Completeness of the UCD Sample

To quantify the completeness of our spectroscopic sample of UCDs, we selected all of the UCD candidates within the central  $60'$  (in geometric average radius) of M87 from the NGVS photometric catalog (Muñoz et al. 2014), based on the  $u^* - i$  vs.  $i - K_s$  diagram (Section 3), size measurement ( $11 \leq r_{\text{h,NGVS}} \leq 50$  pc), and isophotal shapes (SEXTRACTOR ellipticities  $< 0.25$ ). In addition, any obviously extended galaxies were further removed from our final photometric sample.

The completeness in a given magnitude range was determined as the  $\frac{N_{\text{spec}}}{N_{\text{cand}}} \times 100$ , where  $N_{\text{cand}}$  is the number of photometric candidates and  $N_{\text{spec}}$  is the number of candidates with radial velocity measurements. The completeness in different  $g_0$  and  $i_0$  magnitude bins is shown in Figure 4. Overall, our sample is expected to be  $\sim 60\%$  complete at  $g_0 < 21.5$  mag, and  $\sim 55\%$  complete at  $i_0 < 20.5$  mag. In particular, the sample is  $\sim 98\%$  complete at  $g_0 < 20.5$ , which corresponds to  $M_g \leq -10.6$ .

### 5.3. Magnitude vs. Galactocentric Distance

TABLE 1  
SÉRSIC PROFILE FITTING

ID	$g_0$ (mag)	$N_e$ (arcmin $^{-2}$ )	$R_e$ (arcmin)	$n$
(1)	(2)	(3)	(4)	(5)
UCDs	18.5 – 20.5	0.03	12.57	1.43
Blue GCs	18.5 – 24.0	0.87	20.10	3.03
Red GCs	18.5 – 24.0	3.61	5.89	4.26

NOTE. — (1) Population name. (2)  $g$ -band magnitude range of the sample. (3) Surface number density at the effective radius  $R_e$ . (4) Effective radius. (5) Sérsic index.

Figure 5 presents the  $i_0$  magnitude distribution as a function of  $R_{\text{av}}$  from M87. The UCDs, blue GCs and red GCs are plotted as different symbols in Figure 5. We can see that the available observations of GCs within the central  $\sim 5'$  reach down to 22 mag, which is about 1 mag fainter than that at larger radii. We point out that  $\sim 89\%$  of our UCDs have  $i_0 < 20.5$  mag.

### 5.4. Surface Number Density Profiles

As is shown in Figure 4, our sample of UCDs is expected to be nearly 100% complete down to  $g_0 < 20.5$  mag. In Figure 6, we show the radial number density profile of the 59 UCDs with  $g_0 < 20.5$  mag, together with profiles of the blue GCs and red GCs ( $18.5 < g_0 < 24.0$  mag) determined by Durrell et al. (2014). Number density profiles for the surrounding dE galaxies were also shown for comparison. Our specific choice of radial binning for constructing the profile of UCDs ensures that at least 10 data points fall into each radial bin. The vertical error bars of the radial profiles represent the poisson noise. Note that radial profiles of the GCs have been vertically shifted down arbitrarily (2.1 for the blue GCs and 1.7 for the red GCs) for comparison purposes. We point out that the GC surface density profiles derived by Durrell et al. (2014) were based on an adaptive-smoothed GC density maps, with the smoothing kernel FWHM  $\gtrsim 3' - 5'$ . Therefore, the intrinsic surface profiles of GCs in the inner radii may be a little steeper than those shown in Figure 6.

We adopt the Sérsic function (Sérsic 1968; Ciotti 1991; Caon et al. 1993; Graham & Driver 2005) to quantify the radial profiles. Due to the small sample size of sparsely-distributed UCDs, instead of simply fitting the binned profiles, we used the maximum likelihood method (e.g. Kleyna et al. 1998; Westfall et al. 2006; Martin et al. 2008) to estimate the UCD number density profile. Specifically, the likelihood function to be maximized is defined as

$$\mathcal{L}(N_e, R_e, n) \propto \prod_i \ell_i(R_i | N_e, R_e, n) \quad (1)$$

where  $\ell_i(r_i | N_e, R_e, n)$  is the probability of finding the datum  $i$  at radius  $R_i$  given the three Sérsic parameters, i.e. the effective radius  $R_e$ , the number density  $N_e$  at  $R_e$ , and the Sérsic index  $n$ . In particular,

$$\ell_i(R_i | N_e, R_e, n) \propto N_e \exp \left\{ -b_n \left[ \left( \frac{R_i}{R_e} \right)^{1/n} - 1 \right] \right\} \quad (2)$$

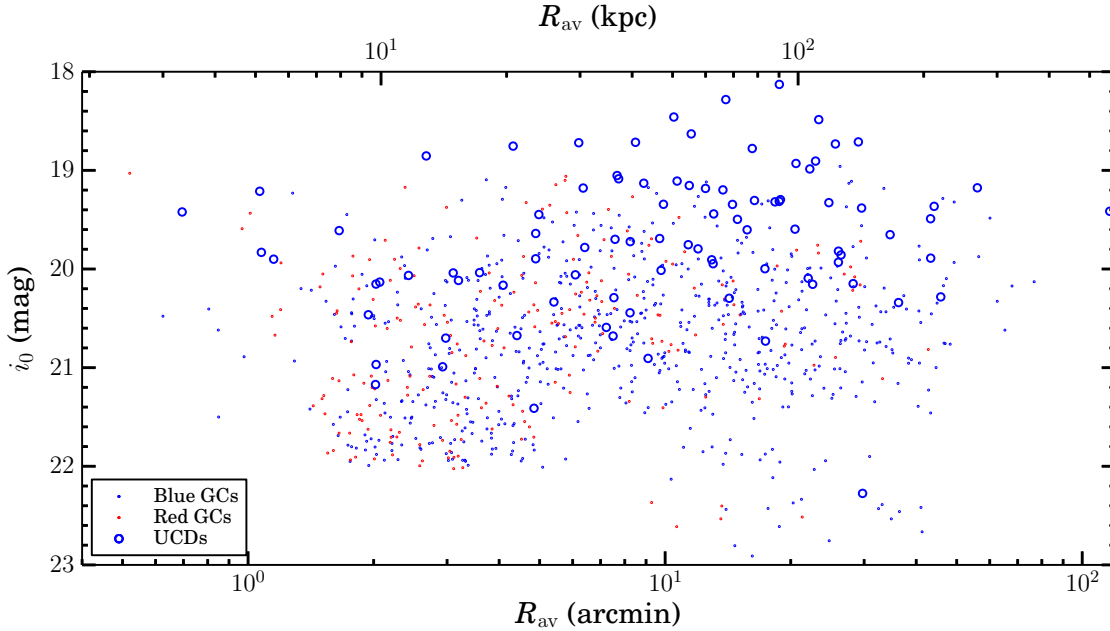


FIG. 5.— Radial distribution of  $i_0$  magnitude for UCDs and GCs.

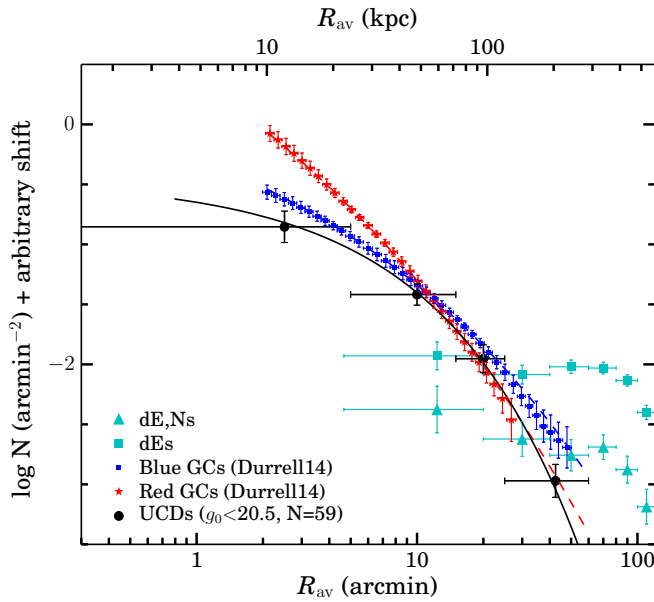


FIG. 6.— Radial surface number density profiles M87 UCDs (black) with  $g_0 < 20.5$  mag. The radial profiles of blue GCs (blue) and red GCs (red) determined by Durrell et al. (2014) were also plotted for comparison. Also over plotted are the number density profiles of surrounding dE galaxies. The profiles of blue GCs and red GCs have been vertically shifted arbitrarily for comparison purpose. Overplotted on the data are the best-fit Sérsic profiles for UCDs, blue GCs and red GCs. Note that our sample of UCDs with  $g_0 < 20.5$  mag is expected to be nearly 100% complete.

where  $b_n$  is a constant that is defined as a function of  $n$  such that  $R_e$  is the effective radius, and we adopted the formula determined by Ciotti & Bertin (1999) to relate  $b_n$  to  $n$ . Furthermore,  $N_e$  can be expressed as a function of  $R_e$ ,  $n$  and the total number of UCDs  $N_{\text{tot}}$  ( $= 59$ ) by integrating the Sérsic profile over the projected area  $\pi R^2$  to the limit radius  $R_{\text{lim}} = 60'$  (e.g. Graham & Driver 2005). Specifically,

$$N_e = \frac{N_{\text{tot}}}{2\pi R_e^2 n \frac{\exp(b_n)}{b_n^2} \gamma(2n, b_n(R_{\text{lim}}/R_e)^{1/n})} \quad (3)$$

where  $\gamma(2n, b_n(R_{\text{lim}}/R_e)^{1/n})$  is the incomplete gamma function. By substituting  $N_e$  from Equation 3 in Equation 1,  $\mathcal{L}$  was maximized to find the most likely parameters  $R_e$  and  $n$  (and thus  $N_e$ ). For the blue and red GCs, we directly fit the Sérsic function to the binned radial profiles shown in Figure 6, which is adequate given the large sample size of the photometric samples of GCs.

The best-fit Sérsic profiles of the three populations are overplotted in Figure 6, and the most likely estimation of the Sérsic parameters is listed in Table 1. The difference between radial profiles of UCDs and GCs is significant. The UCDs have the shallowest radial profiles in the inner  $\sim 15'$  among the three populations, and in the outer radii the profile of UCDs is as steep as that of the red GCs. Previous studies have shown that the surface number density profile of the red GCs closely follow that of the diffuse stellar light (e.g. Geisler et al. 1996; Harris 2009; Durrell et al. 2014). In addition, the surrounding dE galaxies have much flatter and extended number density profiles than UCDs and GCs.

## 6. PHASE-SPACE DISTRIBUTION AND $V_{\text{RMS}}$ PROFILES

Figure 7 gives the radial variation of the line-of-sight velocities of UCDs, GCs and dE galaxies. The blue and red GCs are plotted separately. A  $i$ -magnitude color-coded plot of  $V_{\text{los}}$  vs.  $R_{\text{av}}$  for UCDs is shown in Figure 8.

While we will present a detailed kinematic modeling of the rotation and intrinsic velocity dispersion for our samples in Section 8, it is helpful to first explore variations in the root-mean-square line-of-sight velocity  $v_{\text{rms}}$  as a function of the galactocentric distance from M87 (Figure 9). To construct the  $v_{\text{rms}}$  profiles, we adopted the “sliding bin” method. Specifically, bins of fixed radial width were slid from the center outward, with an offset of  $1'$  between adjacent bins.  $v_{\text{rms}}$  was calculated for data points falling into each individual sliding bin. Considering the lower number density of UCDs and GCs in the larger radii we used different bin widths in different ranges of radii. The bin widths are:  $\Delta R_{\text{av}} = 4'$  for  $R_{\text{av}} < 8'$ ,  $\Delta R_{\text{av}}$



$= 8'$  for  $8' < R_{\text{av}} < 20'$ ,  $\Delta R_{\text{av}} = 12'$  for  $20' < R_{\text{av}} < 40'$ , and  $\Delta R_{\text{av}} = 16'$  for  $R_{\text{av}} > 40'$ .

We require at least 19 data points to be available in each bin when constructing the profiles shown in Figure 9. A biweight  $v_{\text{rms}}$  was calculated for each sliding bin following the methodology of Beers, Flynn, & Gebhardt (1990; cf. Equation 9). The biweight  $v_{\text{rms}}$  estimator is relatively outlier-insensitive, and has proven to be superior to the classical formula when dealing small samples. The 68% confidence interval for  $v_{\text{rms}}$  was estimated by randomly resampling the real data sets without replacement.  $v_{\text{rms}}$  in some fixed radial bins is also overplotted in Figure 9. The dispersion profile for the surrounding dE galaxies is also shown for comparison.

As shown in Figure 9, the UCDs follow a velocity dispersion profile more similar to that of the blue GCs than the red GCs. The  $v_{\text{rms}}$  of blue GCs beyond  $30'$  increases steeply to reach  $\sim 500 \text{ km s}^{-1}$ . The red GCs have an overall lower velocity dispersion than the UCDs and blue GCs. The blue GCs and UCDs show a slight increase in velocity dispersion between  $\sim 4'$  and  $12'$ , whereas the red GCs do not clearly show such a “hot” feature. This may suggest the existence of “hot” substructures which have not yet reached an dynamical equilibrium state, as suspected by Zhu et al. (2014).

We note that the rising  $v_{\text{rms}}$  of the blue GCs beyond  $\sim 30'$  should not be regarded as signifying a transition to the general cluster potential, because the rising dispersion is mostly driven by a larger scatter of  $V_{\text{los}}$  toward the low-velocity side of the systemic velocity of M87 (see Figures 7 and 17), and the majority of the blue GCs out to  $R \sim 40'$  ( $\sim 190 \text{ kpc}$ ) are actually tightly clustered around the systemic velocity of M87. A low-velocity excess (toward the North West of M87; Figure 19) is also present in the velocity distribution of dwarf galaxies locally surrounding M87 (Binggeli, Popescu & Tammann 1993). So an excess of low-velocity GCs beyond  $\sim 30'$  indicates a significant contamination from the intra-cluster population of GCs projected along the line of sight.

Moreover, beyond the central  $\sim 30'$ , the GCs that are clustered around the systemic velocity of M87 tend to have redder colors than those with lower velocities. If we only consider relatively “red” blue GCs, say those with  $(g - i)_0 > 0.75$ , the resultant  $v_{\text{rms}}$  of the 22 GCs between  $30'$  and  $60'$  is  $252_{-59}^{+38} \text{ km s}^{-1}$ , whereas for the other 32 blue GCs with  $(g - i)_0 < 0.75$  the corresponding velocity dispersion is  $524_{-34}^{+42} \text{ km s}^{-1}$ . Since lower luminosity galaxies have on average bluer colors than higher luminosity galaxies for both their blue and red GC systems (e.g. Peng et al. 2006), it is quite plausible that the high-dispersion “bluer” GCs are overwhelmingly contaminated in projection by the intra-cluster populations that have been tidally stripped from dwarf galaxies, whereas the relatively “redder” GCs trace the underlying potential of M87 more faithfully. This suggests that the stellar halo of M87 extends beyond, instead of being truncated at (Dopherty et al. 2009),  $R_{\text{av}} \sim 150 \text{ kpc}$ .

## 7. VELOCITY DISTRIBUTION

The line-of-sight velocity distribution is shaped by the global kinematics of a system. Figure 10 presents the line-of-sight velocity histograms (with the systemic velocity of M87 being subtracted) of UCDs (left), blue GCs (mid-

dle) and red GCs (right). We show the bright and faint subsamples in Figures 11. The bin size of the histograms is  $50 \text{ km s}^{-1}$ , which was chosen to be larger than the typical measurement uncertainties. The red curve overplotted on each histogram is the adaptive kernel density estimation (KDE) of the velocity distribution. The KDE was constructed through a Gaussian-shaped kernel, with the Gaussian  $\sigma$  being equal to the measurement uncertainty for each data point, and we further smoothed the resultant KDE with a Gaussian of  $\sigma = 20 \text{ km s}^{-1}$  ( $\sim 1/2.35 \times$  the bin size of the histograms). Also overplotted on each histogram as dashed blue curve is a scaled Gaussian distribution, with the Gaussian  $\sigma$  being equal to the standard deviation of the observed distribution.

To quantify the overall shape of the velocity distribution, we calculated the standard deviation  $\sigma$ , skewness  $G_1$ , and the kurtosis  $G_2$ , and they are listed on the top of each panel in Figures 10, and 11. The skewness was calculated as the ratio of the third cumulant and the 1.5th power of the second cumulant, and the kurtosis was calculated as the ratio of the fourth cumulant and the square of the second cumulant. For small samples, skewness and kurtosis defined by cumulants are relatively unbiased compared to the traditional definitions with moments. A Normal distribution has both the skewness and kurtosis equal to zero, and a distribution with sharper peak and (especially) heavier tails has more positive kurtosis.

The estimation of kurtosis is sensitive to extreme outliers. A meaningful estimation of kurtosis should reflect the overall shape of a distribution, instead of being driven by few extreme outliers. To obtain a robust estimation of kurtosis, we adopted a “ $\sigma$ -clipping” method in the kurtosis space. Specifically, for a data set of  $N$  points, we resampled the original data set  $N$  times (without replacement), with one different data point being taken out each time, similar to the technique of jackknife resampling. If the resultant kurtosis after taking out a given data point is more than  $5\sigma$  away from the mean, that data point is regarded as an outlier. This “ $\sigma$ -clipping” process was iterated until no further outlier was found. Among the full samples within  $R < 30'$  (Section 7.1), 2 UCD (2%), 13 blue GCs (2%) and 5 red GC (2%) were found to be outliers for kurtosis estimation. The clipped outliers are mostly the extreme velocities in our samples, and it is quite possible that most of these outliers belong to the intra-cluster population of the Virgo cluster.

As a fourth-moment measurement, it is not surprising that the standard kurtosis largely reflects the tail behavior. A complete description of the shape properties of a distribution should involve both the tailedness and peakedness. An outlier-insensitive, quantile-based alternative for the standard kurtosis, i.e. the  $T$  parameter, was introduced by Moors (1998), and this alternative definition is expected to be more sensitive to the peakedness than  $G_2$ . A detailed introduction about  $T$  is given in the Appendix. The  $T$  parameter is defined such that a Normal distribution has a  $T$  equal to 0, and a positive  $T$  indicates heavier tails and (especially) a sharper peak than a Normal distribution.

The  $\sigma$ ,  $G_1$  and  $G_2$  reported below were calculated based on outlier-rejected samples. The 68% confidence intervals for all the above mentioned shape parameters, including the  $T$  parameter, were determined with by ran-

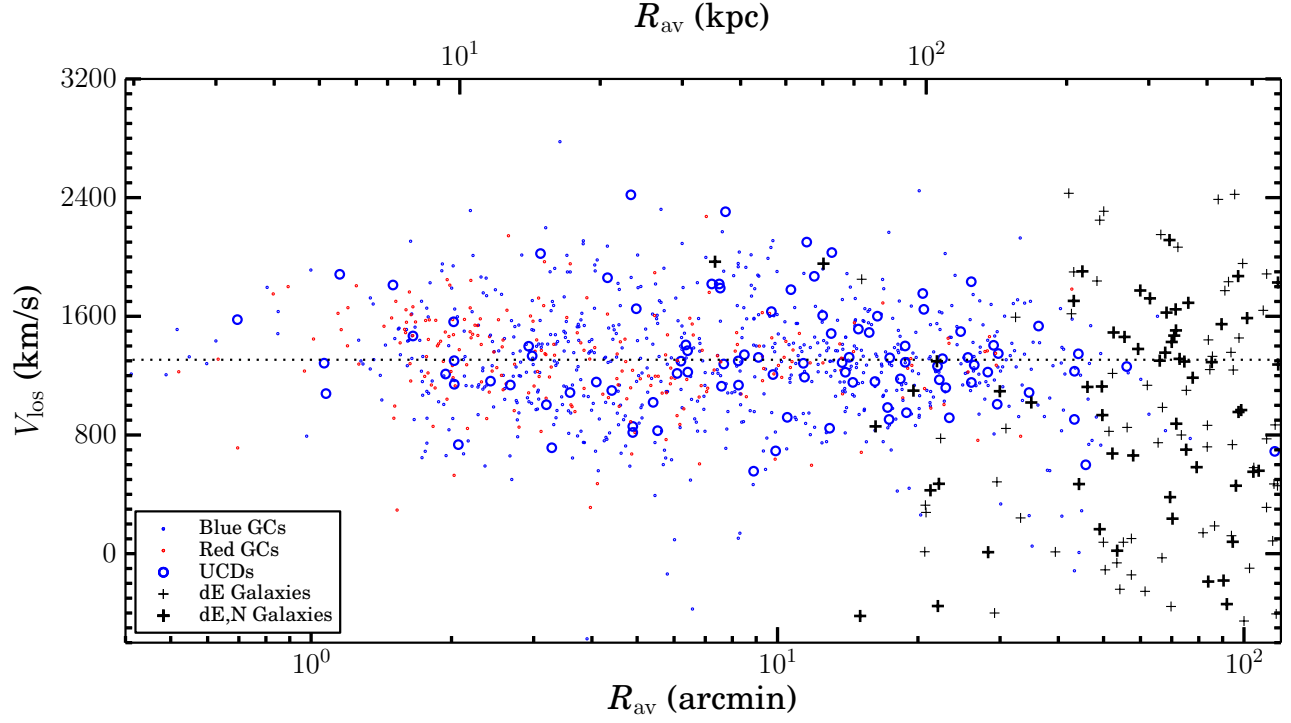


FIG. 7.— The line-of-sight velocities vs. the geometric average radius from M87. The UCDs, blue GCs, red GCs, and dE galaxies (non-nucleated and nucleated) are plotted separately as different symbols. The horizontal dotted line marks the systemic radial velocity of  $1307 \text{ km s}^{-1}$  for M87 (Binggeli et al. 1993).

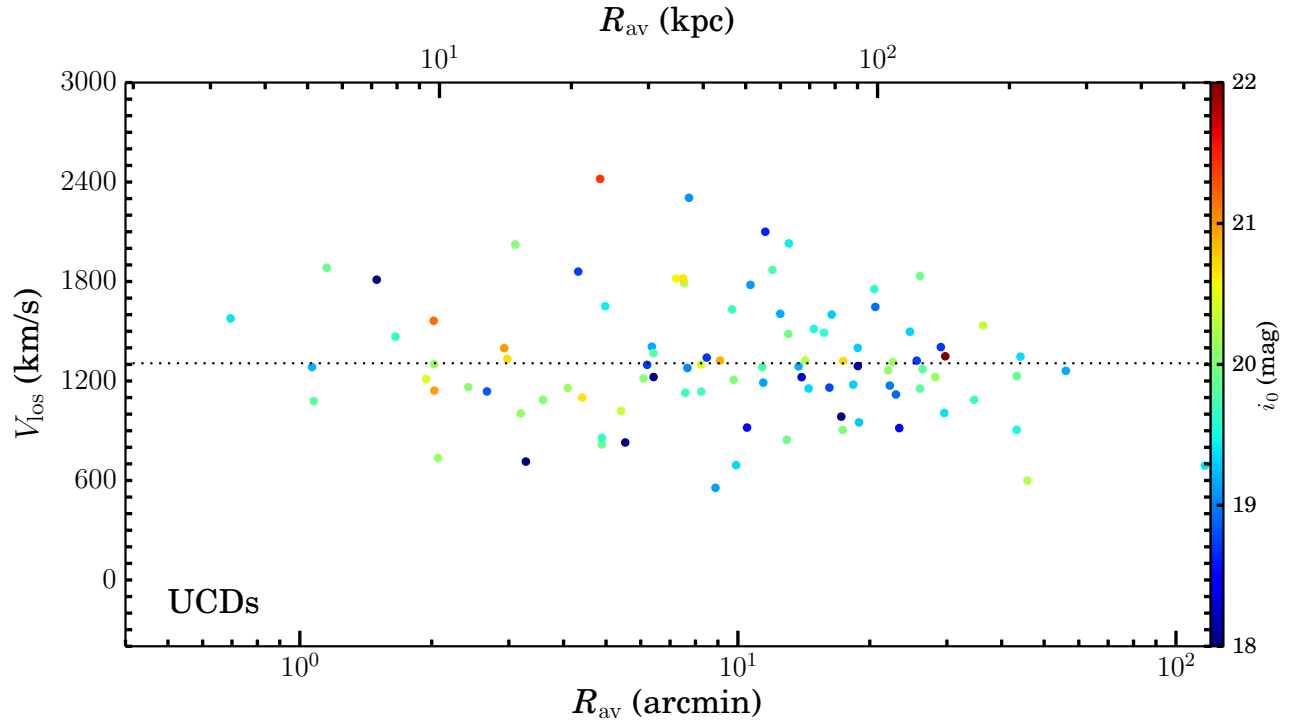


FIG. 8.— The UCD line-of-sight velocities vs. the geometric average radius from M87. Here different UCDs are color-coded with their  $i_0$  magnitude. The horizontal dotted line marks the systemic radial velocity of  $1307 \text{ km s}^{-1}$  for M87.

domly resampling the real data sets. The estimated  $G_2$  and  $T$  for some specified radial bins are listed in Tables 2, 3, and 4.

### 7.1. The Full Samples

The UCDs and blue GCs have similarly higher dispersion in the velocity distribution than the red GCs. The velocity distribution of UCDs is skewed toward the higher velocity tail, as quantified by a positive skewness, whereas the distribution of red GCs is skewed toward the lower velocity tail, as quantified by a negative skewness. The skewness difference between the three populations is partly reflected in their different systemic velocities  $V_{\text{sys}}$  (Table 2). The velocity distribution of UCDs is noticeably sharper than a Gaussian (blue dashed curves in Figure 10), whereas the velocity distributions of GCs are only marginally sharper than a Gaussian. The different sharpness of the three distributions is well reflected in their different  $T$  parameters. In addition, the UCDs and blue GCs have a similarly negative  $G_2$ , suggesting slightly lighter tails than a Gaussian. As we will show later (Section 9), the peaky velocity distribution of UCDs is consistent with a radially-biased velocity dispersion tensor at large galactocentric distances, whereas the lighter tails are in line with a tangentially-biased velocity dispersion tensor at small distances.

### 7.2. Bright and Faint Subsamples

Since there are only 11 UCDs at  $i_0 > 20.5$  mag, the calculation of skewness and kurtosis for these faint UCDs is subject to large uncertainties and bias, and will not be discussed further. For the blue GCs, the bright and faint subsamples have similar velocity dispersion. Nevertheless, the bright blue GCs have much more negative  $G_2$  and marginally lower  $T$  than the faint ones. For the red GCs, the bright subsample has a significantly smaller (by  $\sim 70 \text{ km s}^{-1}$ ) velocity dispersion and larger  $G_2$  than the faint subsample.

Most of the confirmed GCs with  $i_0 \gtrsim 21.5$  mag were observed by S11 with the Low Resolution Spectrometer (LRIS) on Keck. The Keck/LRIS survey of S11 only covered the central  $\sim 1.5 - 5.5'$  of M87, and as a result the confirmed faint GCs are primarily located in the central region (Figure 5). To check if the velocity distribution differences between the bright and faint GCs are driven by the observational bias in spatial coverage for the sample of faint GCs, we derived the shape parameters of the velocity distribution for the bright and faint GCs within the central  $5'$ . It turns out similar differences between the bright and faint subsamples still exist for both the blue and red GCs.

Furthermore, previous studies (S11; Agnello et al. 2014) found that the M87 GCs of different colors may exhibit different kinematical properties. So we also checked for any possible color bias for the bright and faint subsamples. The median  $(g - i)_0$  colors of the bright and faint blue GCs are 0.76 and 0.74 respectively, suggesting that there is no significant color bias for the bright and faint subsamples. For the red GCs, the median  $(g - i)_0$  colors of the bright and faint subsamples are 0.95 and 1.00 respectively. When we divide the red GCs into two  $(g - i)_0$  color groups with a division color of 0.97, the above mentioned difference still exist for subsamples in

each color group, although there is a systematic difference between the “bluer” and “redder” groups, in the sense that the corresponding subsamples in the “bluer” group have about  $\sim 70 \text{ km s}^{-1}$  lower velocity dispersion than those in the “redder” group.

### 7.3. Radial Trend of Kurtosis of the blue GCs

The large sample size of the blue GCs allows us to explore the radial trend of the shape parameters for the velocity distribution. Figure 12 shows the kurtosis for the bright and faint blue GCs in three fixed radial bins, namely  $0'-4'$ ,  $4'-12'$ , and  $12'-30'$ . It is significant that the bright subsamples have systematically lower kurtosis than the faint ones.

### 7.4. Interpretation: from kurtosis to orbital anisotropies

For a given number density profile, there is a one-to-one relationship between the kurtosis and the orbital anisotropy parameter  $\beta$  ( $\equiv 1 - \sigma_t^2 / 2\sigma_r^2$ , where  $\sigma_t$  and  $\sigma_r$  are the tangential and radial components of the velocity dispersion ellipsoid; positive (negative)  $\beta$  corresponds to radially (tangentially) anisotropic orbital structures), under the assumption that the velocity dispersion and  $\beta$  are constant with galactocentric radius (Napolitano et al. 2009). Napolitano et al. (2009) found that  $\beta$  can be directly estimated through deprojection of observables involving the kurtosis of  $V_{\text{los}}$  and volume number density profiles of the tracer population (see the formulae B10, B11 and B12 in Napolitano et al. 2009).

With the kurtosis and surface density profiles  $^\dagger$  (parameterized as Sérsic functions, Section 5.4) in hand, the average  $\langle \beta \rangle$  for UCDs, blue GCs and red GCs were estimated (through numerical integration from one effective radius to infinity for each of the three populations, also listed in Tables 2, 3, and 4) to be  $-0.3^{+0.3}_{-0.4}$ ,  $-0.3^{+0.2}_{-0.2}$ , and  $0.2^{+0.1}_{-0.1}$  respectively for the full samples. For the bright subsamples, the corresponding  $\langle \beta \rangle$  are  $-0.3^{+0.3}_{-0.4}$ ,  $-1.0^{+0.3}_{-0.4}$ , and  $0.2^{+0.2}_{-0.2}$  for the UCDs, blue GCs and red GCs respectively; For the faint subsamples, the  $\langle \beta \rangle$  are estimated to be  $-0.1^{+0.1}_{-0.2}$  and  $0.7^{+0.1}_{-0.1}$  for the blue and red GCs respectively. We emphasize that the adopted approach to calculate  $\beta$  is only strictly applicable to a constant velocity dispersion profile which is not true for either of our three populations, so our estimation of  $\beta$  here should be regarded at most as a zeroth-order approximation of the average  $\langle \beta \rangle$ . Later in this paper (Section 9), we will solve the Jeans equations for the radial profiles of  $\beta$ .

Taken at face value, among the three populations, the red GCs have on average the highest radial anisotropy, whereas the blue GCs have the lowest radial anisotropy. In addition, the faint subsamples tend to have higher radial anisotropies than the bright subsamples. Given the good correspondence between kurtosis and  $\langle \beta \rangle$ , the radial kurtosis profiles shown in Figure 12 indicate

$^\dagger$  To deproject the observed surface number density profiles  $N_R$  to volume number density profiles  $n_r$ , we assumed a spherically symmetric geometry, which gives

$$n_r \propto \int_r^\infty \frac{dN_R}{dR} \frac{dR}{\sqrt{R^2 - r^2}} \quad (4)$$

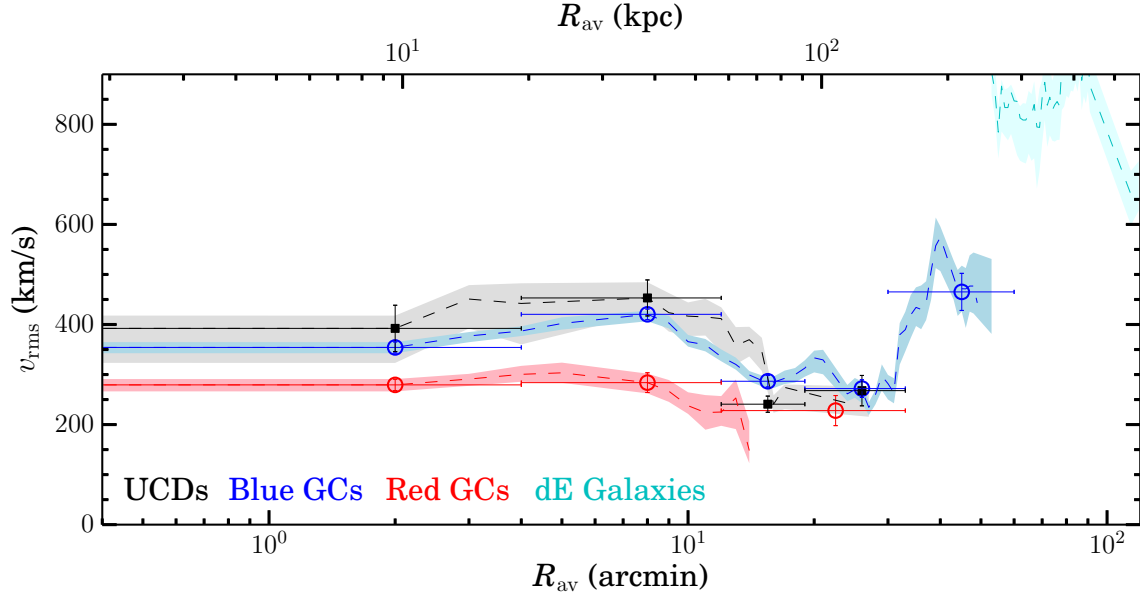


FIG. 9.— Radial variations of the rms velocities of UCDs, blue GCs, red GCs and dE galaxies. The profiles were constructed by sliding bins of fixed radial widths ( $\Delta R_{\text{av}} = 4'$  for  $R_{\text{av}} < 8'$ ;  $\Delta R_{\text{av}} = 8'$  for  $8' < R_{\text{av}} < 20'$ ;  $\Delta R_{\text{av}} = 12'$  for  $20' < R_{\text{av}} < 40'$ ;  $\Delta R_{\text{av}} = 16'$  for  $R_{\text{av}} > 40'$ ), with a step of  $1'$  between adjacent sliding windows. The solid curves correspond to the calculated  $v_{\text{rms}}$ , and the shaded regions mark the 68% confidence limits. To be used in constructing the profiles, at least 19 data points should be available for a given radius bin.

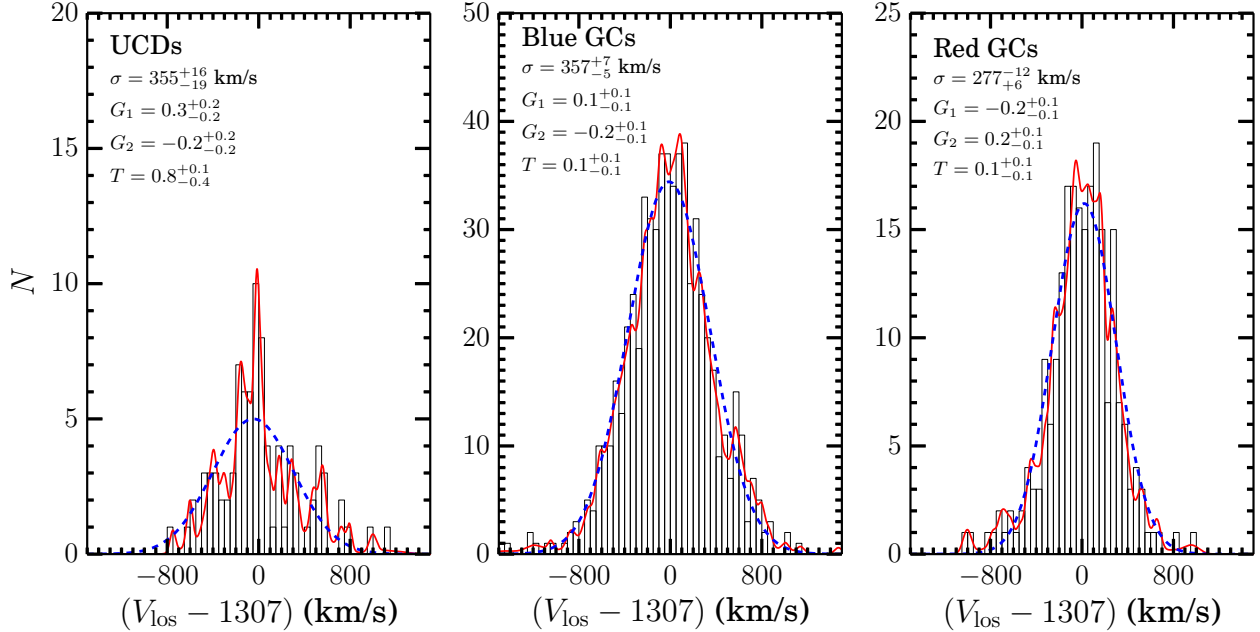


FIG. 10.— The line-of-sight velocity distribution of the UCDs (left), blue GCs (middle) and red GCs (right) in the inner  $30'$  of M87. The histograms have a bin width of  $50 \text{ km s}^{-1}$ . The red solid curve overplotted on each histogram is the kernel density estimation of the observed distribution, and the blue dashed curve represents a Gaussian distribution, with the Gaussian  $\sigma$  being equal to the standard deviation of the velocity distribution. Note that the Gaussian distributions have been scaled by the area under the histograms. The standard deviation  $\sigma$ , skewness  $G_1$ , kurtosis  $G_2$  and  $T$  parameter (see the Appendix for the definition) were also listed on the top of each panel. Note that, the UCDs have a sharper velocity distribution than the Gaussian, whereas the GCs (especially the blue GCs) have overall close-to-Gaussian distributions.

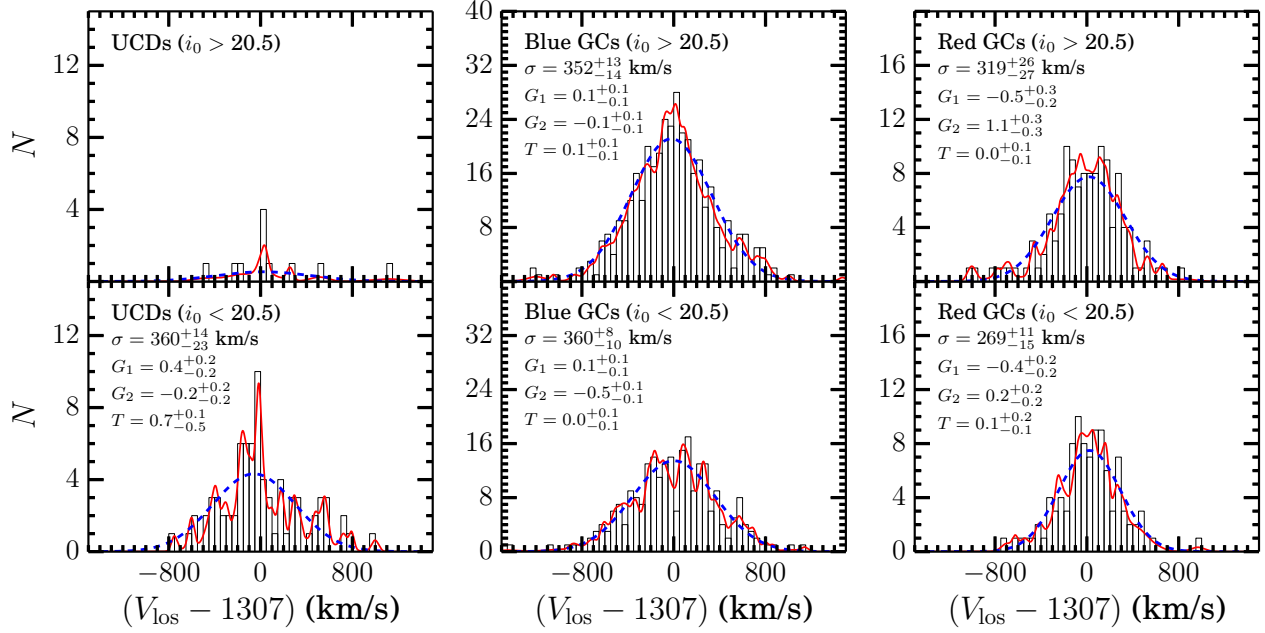


FIG. 11.— The line-of-sight velocity distribution of the subsamples of bright (lower panels) and faint (upper panels) UCDs (left), blue GCs (middle) and red GCs (right). The histograms have a bin width of  $50 \text{ km s}^{-1}$ . The red solid curve overplotted on each histogram is the kernel density estimation of the observed distribution, and the blue dashed curve represents a Gaussian distribution, with the Gaussian  $\sigma$  being equal to the standard deviation of the velocity distribution. Note that the Gaussian distributions have been scaled by the area under the histograms. The standard deviation  $\sigma$ , skewness  $G_1$ , kurtosis  $G_2$  and  $T$  parameter were also listed on the top of each panel.

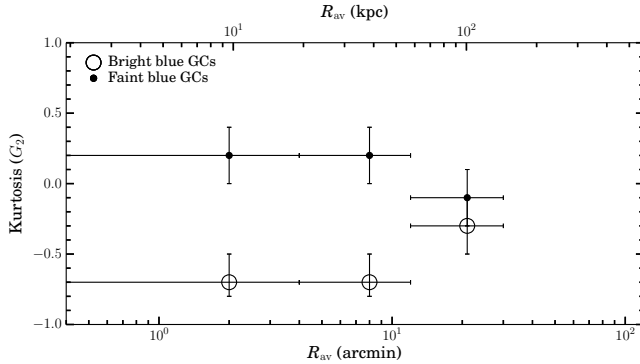


FIG. 12.— Radial variation of velocity Kurtosis of the bright (large open circles) and faint (small filled circles) blue GCs.

that the faint blue GCs are more radially-biased than the bright ones.

## 8. KINEMATIC MODELING

### 8.1. Methodology

Under the assumption that the intrinsic angular velocity of a system, of either GCs or UCDs, is only a function of the galactocentric distance  $r$ , the (projected) average line-of-sight velocities vary sinusoidally with the projected azimuth  $\theta$  (e.g. Côté et al. 2001). As a consequence, it is customary to fit the line-of-sight velocities of GC and UCD systems with sine or cosine curves as a function of projected azimuth  $\theta$ , in order to determine the rotation amplitude and rotation axis (e.g. Cohen & Ryzhov 1997; Kissler-Patig & Gebhardt 1998; Côté et al. 2001; S11; Pota et al. 2013). Assuming Gaussian distributions for both the measurement uncertainties and the intrinsic velocity dispersions, the likelihood of a model

fit to given observations (e.g.  $v_i \pm \Delta v_i$ ) is:

$$\mathcal{L} \propto \prod_i \frac{1}{\sqrt{\sigma_p^2 + \Delta v_i^2}} \exp \left[ -\frac{1}{2} \frac{(v_i - v_{\text{mod}})^2}{\sigma_p^2 + \Delta v_i^2} \right]. \quad (5)$$

where  $\sigma_p$  is the intrinsic (projected) velocity dispersion, and

$$v_{\text{mod}} = v_{\text{sys}} + v_{\text{rot}} \sin(\theta - \theta_0) \quad (6)$$

with  $\theta_0$  being the position angle (PA, measured east of north) of the rotation axis. Maximization of Equation 4 is equivalent to minimizing the  $\chi^2$  statistic (e.g. Bergond et al. 2006):

$$\chi^2 = \sum_i \left\{ \frac{(v_i - v_{\text{mod}})^2}{\sigma_p^2 + (\Delta v_i)^2} + \ln [\sigma_p^2 + (\Delta v_i)^2] \right\} \quad (7)$$

By minimizing Equation 7 for a given dataset, we can determine the systemic velocity  $v_{\text{sys}}$ , rotation amplitude  $v_{\text{rot}}$ , rotation axis  $\theta_0$  and the intrinsic velocity dispersion  $\sigma_p$ . Note that we have assumed the kinematic axis ratio  $q$  to be 1 when writing Equation 6 in order to be consistent with previous kinematical studies of M87 GCs (e.g. Côté et al. 2001; S11). The results are essentially the same when fixing  $q$  to the photometric axis ratio of the diffuse stellar light. Considering the possible (unknown) inclination of the rotation axis with respect to the plane of sky,  $v_{\text{rot}}$  determined here should be regarded as a lower limit. To estimate the uncertainties of the fitted parameters, we randomly resampled the real dataset and repeated the kinematic fitting to the resamples, and then obtained the 68% confidence intervals from the resultant parameter distribution.

### 8.2. Bias and Significance

Kinematics fitting to discrete data points tends to overestimate the intrinsic rotation, and the degree of overestimation or bias depends on the sample size, the azimuthal distribution of data points, and the importance of rotation as compared to the dispersion (e.g. Sharples et al. 1998; Romanowsky et al. 2009; S11). Reliability of the fitted rotation amplitudes can be quantified in two mutually related ways, one is the most likely level of bias, and the other one is the significance (or confidence level, CL) of the fitted rotation.

*Bias.* To check the level of bias for the best-fit rotation, we first constructed a series of kinematic models for each of the three populations, with the rotation amplitudes varying from 0 to 250 km s<sup>-1</sup> and the other kinematic parameters being fixed at their best-fit values from the real data sets. Then, starting from each of these kinematic models, velocities at each observed GC or UCD location were randomly drawn from a normal distribution, with the variance being equal to a quadrature combination of the velocity dispersion and measurement uncertainties. In particular, at each input rotation amplitude, 5000 Monte Carlo samples were generated for each population, and the standard kinematic fitting (Section 8.1) was carried out for these mock samples. Lastly, for each *input* rotation amplitude, we determined the median of the corresponding 5000 best-fit *output* rotation amplitudes, and this defines a one-to-one relation between the *input* and the most likely *output*, which can be used to estimate the most probable bias in our best-fit rotation for the real data sets.

*Significance.* we follow the procedure first introduced by Sharples et al. (1998) to estimate the CL of our best-fit rotation amplitudes (see also Romanowsky et al. 2009). In particular, for each of the three populations, we randomly shuffled the position angles of the observed data points for 5000 times, and repeated the kinematics fitting to each realization. A random shuffling of the position angles can erase (if any) signatures of any possible rotation. Therefore, if the percentage of random realizations that lead to fitted rotation amplitudes greater than or equal to the best-fit value  $v_{\text{rot}}$  for the real data set is  $p$ , then the confidence level of  $v_{\text{rot}}$  can be estimated as  $1 - p$ . In this paper, confidence levels  $> 90\%$  are regarded to be significant.

### 8.3. Global Kinematics

#### 8.3.1. The Full Samples

Figure 13 shows the azimuthal variation of line-of-sight velocities for all M87 UCDs within the central 30', along with the blue GCs and red GCs for comparison. Overlaid on the data in each panel is the best-fit sine curves. The fitting results are summarized in Table 2. The UCDs and blue GCs have similar intrinsic velocity dispersion. The rotation amplitude of UCDs is more than 4 (2) times stronger than that of the blue (red) GCs. Additionally, the rotation axis of UCDs is roughly orthogonal to that of blue GCs. It is interesting that the red GCs, which have a smaller velocity dispersion than the UCDs and blue GCs, have a rotation axis that is more aligned with the UCDs rather than the blue GCs. Our best-fit parameters for the blue and red GCs are generally consistent with those determined by S11 (see their Table 14) within the mutual uncertainties. Note that the rotation angles reported by

S11 are the direction of maximum rotation amplitude, which is 90° offset from the angular momentum vector. In addition, the kinematics parameters reported by S11 were already bias-corrected.

Following the procedure described in Section 8.2, we estimated the most likely bias and the significance (or CL) of our best-fit rotation amplitudes, and the results are shown in Figure 14 and Table 2. According to bias test, the intrinsic rotation amplitude for UCDs is most probably overestimated by  $\sim 10$  km s<sup>-1</sup>, for blue GCs  $\sim 6$  km s<sup>-1</sup>, and for red GCs  $\sim 1$ –2 km s<sup>-1</sup>. As to the confidence levels, the probability that we found a rotation amplitude greater than or equal to the best-fit value for UCDs purely by chance is  $\sim 2\%$  (CL = 98%), the probability is  $\sim 27\%$  (CL = 73%) for blue GCs, and  $\sim 12\%$  (CL = 87%) for red GCs.

Surface fitting to the spatial distribution (within the inner 30') of line-of-sight velocities is presented in Figure 15 as a color-coded background for each of the three populations. The data points over plotted on the fitted surface are also color-coded according to their individual line-of-sight velocities. In order to bring out details of the fitted surface, individual data points with velocities  $> 1550$  km s<sup>-1</sup> or  $< 1050$  km s<sup>-1</sup> were not distinguished in colors from those with velocities = 1550 km s<sup>-1</sup> or = 1050 km s<sup>-1</sup> respectively. The surface fitting was carried out with the Kriging technique as implemented in R package `FIELDS`. The Kriging technique has been recently used for exploring the velocity field of GC systems (e.g. Foster et al. 2013) and the galactic spatial distribution of metallicities (e.g. Pastorello et al. 2014). Instead of simply applying an inverse distance weighting, Kriging takes into account both the spatial configuration and covariances of the dataset when assigning weights to neighboring data points for interpolation. In this work, the spatial covariance is assumed to be an exponential function of separation distance, and the smoothing parameter  $\lambda$  was fixed. The global rotation axes determined from our kinematics fitting were indicated as red arrows in Figure 15, and the arrow length is proportional to the best-fit rotation amplitude.

Our global kinematics fitting is essentially driven by the clustering trend of  $V_{\text{los}}$  along the azimuthal direction, and primarily reflects the velocity field in the central region where most data points are located. Accordingly, as shown in Figure 15, there is generally a good match between the direction of arrows and the fitted Kriging velocity field in the central regions. The Kriging surface fitting is driven by the overall data configuration and spatial covariance, and in particular, by definition it is not influenced/biased by spatial clustering of data points. Of the three populations, the blue GCs have an overall velocity field that seems to be more closely aligned with the photometric major axis, while the UCDs have a velocity field in better agreement with that of the red rather than the blue GCs.

The significantly stronger rotation of UCDs as compared to the GCs suggests that the UCDs are kinematically distinct from the GCs. The smaller velocity dispersion of red GCs is in agreement with the fact that red GCs are more centrally concentrated than the blue GCs and UCDs (Figure 6). Similar to the blue GCs, a more or less minor axis rotation was also recently detected from integrated stellar-light spectra in the central



one effective radius of M87 (e.g. Arnold et al. 2013). In addition, a twist of the velocity field within the central half arc minute was recently reported by Emsellem, Krajnović & Sarzi (2014) based on IFU spectra of the integrated stellar light. The misaligned velocity field across different radii and among different kinematic tracers (e.g. UCDs vs. GCs) all suggest that the halo of M87 is most probably triaxial, instead of being axisymmetric (e.g. Schwarzschild 1979; Statler 1991; Franx, Illingworth & de Zeeuw 1991; van den Bosch et al. 2008; Hoffman et al. 2009; Emsellem, Krajnović & Sarzi 2014).

### 8.3.2. The Bright and Faint Subsamples

In this subsection, we explore the possible differences in global kinematics between the bright and faint subsamples. The relevant kinematic fitting results are summarized in Tables 3 and 4. Figure 16 shows the azimuthal variation of line-of-sight velocities for the bright and faint subsamples of UCDs and GCs separately. Again, the best-fit sine curves are overlaid on the data points. For the blue GCs, no significant rotation was found for either the bright or faint ones. The bright red GCs exhibit a significantly lower (by  $\sim 50 \text{ km s}^{-1}$ ) velocity dispersion and much less significant rotation than the faint subsample. The sample size of faint UCDs is too small to give meaningful kinematic parameters. The kinematic parameters of the bright UCDs resemble those of the full sample.

### 8.4. Radial variation of Kinematics

Radial variation of the kinematic parameters ( $\theta_0$ ,  $v_{\text{rot}}$ , and  $\sigma_p$ ) is presented in Figure 18. Fitting results for data points falling into some fixed radial range are listed in Tables 3 and 4. The way that we constructed the profiles in Figure 18 is the same as in Section 6 which presents the  $v_{\text{rms}}$  profiles (Figure 9). Basically, we performed kinematic fitting to data points that fall into each individual sliding radial bin. Figure 17 shows the azimuthal variations of line-of-sight velocities of UCDs (the left column), blue GCs (the middle column) and red GCs (the right column) in five different elliptical annuli. The five annuli were selected to be representative of the key features in the radial profiles of the UCD kinematics (Figure 18). Note that the kinematic parameters plotted in Figure 18 are not corrected for possible bias.

Based on Figure 18 and Table 2, the UCDs and blue GCs have similar  $\sigma_p$  profiles.  $\sigma_p$  of the red GCs is systematically lower than the other two populations across the full radius range. The strongest rotation of UCDs is found around  $R_{\text{av}} \sim 8' - 16'$ , where the rotation axis is similar to the full sample of UCDs. The blue GCs exhibit insignificant rotation across the full radius range, whereas the red GCs show marginally significant rotation around  $\sim 10'$ . We note that, in the Kriging maps shown in Figure 15, a weak, but visible, gradient along the photometric major axis can be seen for blue GCs beyond the central  $\sim 5'$ , suggesting that the usual one-dimensional kinematics fitting ( $V_{\text{los}}$  vs. PA) and the two-dimensional surface fitting are complementary to each other. The seemingly strong rotation for blue GCs beyond the central  $30'$  turns out to be not significant.

The relevant kinematic parameters for the bright and faint subsamples of GCs in some specified radial bins are listed in Tables 3 and 4 separately. No significant rotation

was found across the full radius range for both the bright and faint GC subsamples.

Lastly, we checked the color-magnitude distribution of the UCDs in the radius range ( $10' - 20'$ ) where the strongest rotation was found, and it turns out that these UCDs follow a color-magnitude relation indistinguishable from the whole sample. This suggests that the strong rotation most probably reflects the global kinematics of the UCD system.

### 8.5. Velocity Field of the Surrounding dEs

The Virgo core region is still dynamically young (e.g. Binggeli et al. 1987). Deep wide-field optical imaging toward the core region revealed a complex network of extended tidal features surrounding M87 and other giant ellipticals (e.g. Mihos et al. 2005; Janowiecki et al. 2010), suggesting an ongoing hierarchical assembly of the Virgo core. It is thus natural to look for any connection between the velocity field of surrounding dwarf galaxies and stellar clusters in M87. Figure 19 presents the velocity field for 69 non-nucleated (*left panel*), 59 nucleated (*middle panel*) and all (*right panel*) dE galaxies within  $2^\circ$  of M87. As in Figure 15, Kriging maps of the mean velocity fields are color-coded in Figure 19, and the individual data points follow the same color scheme. There is no significant difference between the direction of velocity gradients of nucleated and non-nucleated dEs. The direction of the velocity gradients of dEs more or less follows the photometric major axis of M87. Among the three velocity fields shown in Figure 15, the blue GCs seem to match the dEs best, in general agreement with Côté et al. (2001).

We note that the remarkable velocity gradient on the Kriging maps of dEs is primarily driven by an excess of low-velocity dEs toward the north west direction. These excess low-velocity dEs are most probably associated with a small subcluster of galaxies (e.g. Binggeli et al. 1993; Schindler, Binggeli, & Bohringer 1999; Jerjen, Binggeli, & Barazza 2004) centered on M86, which has a radial velocity  $\simeq -244 \text{ km s}^{-1}$  and is about 1 Mpc more distant than M87 (Mei et al. 2007). It is no doubt that the M87 subcluster and M86 subcluster are moving toward each other, and an imminent merging between the two of them has long been speculated (e.g. Bohringer et al. 1994; Binggeli et al. 1993).

### 8.6. Interpretation: Ongoing Accretion of Dwarf Galaxies?

The observation that the surrounding dEs (especially the non-nucleated ones) follow a similar velocity field to the GCs (especially the blue ones) is consistent with the scenario that the GC systems, especially the metal-poor ones, may have been primarily assembled by accreting satellite dwarf galaxies along the photometric major axis of M87 (e.g. Côté, Marzke & West 1998). In line with this ongoing accretion or infalling picture, West & Blakeslee (2000) found that Virgo's brightest ellipticals have a strong collinear arrangement in three dimensions. This so-called "principal axis", which appears to join a filamentary bridge of galaxies connecting the Virgo cluster to Abell 1367 and passes through the Virgo core, is also more or less aligned with the major axes of Virgo's ellipticals (including M87). This "princi-

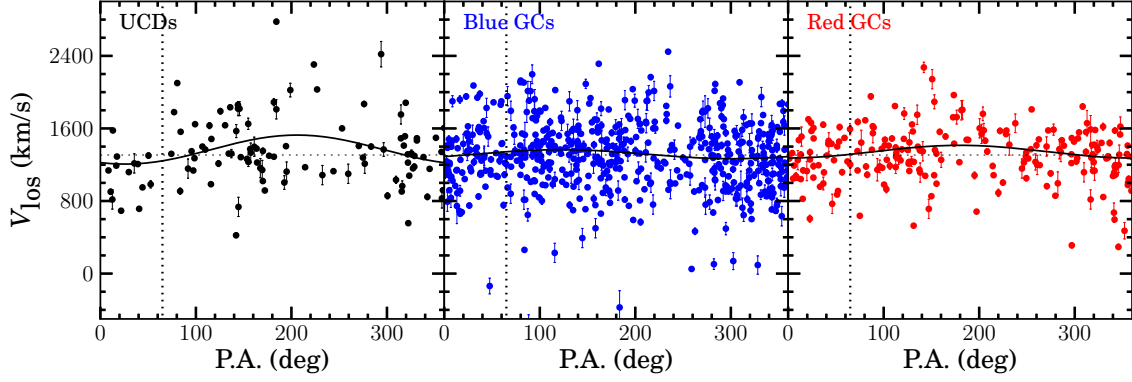


FIG. 13.— The line-of-sight velocity variations as a function of PA (East of North) for the full samples of UCDs (left), blue GCs (middle), and Red GCs (right). Overlaid on the data in each panel is the best-fit sine curve. The horizontal dotted lines mark the systemic radial velocity of  $1307 \text{ km s}^{-1}$  of M87, and the vertical dotted lines mark PA of the photometric minor axis of M87.

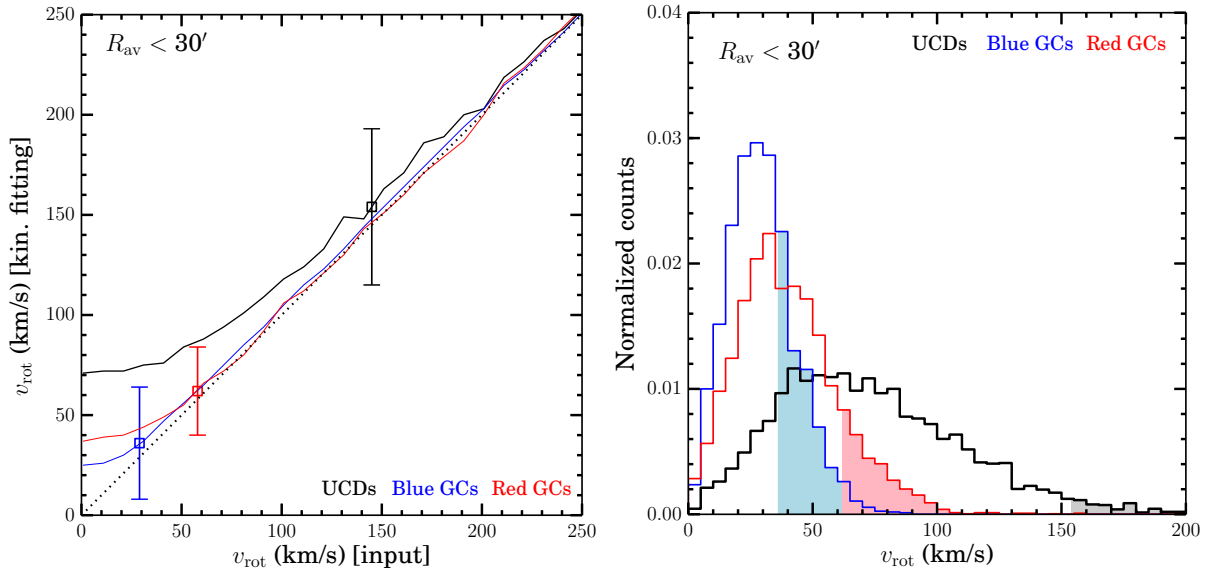


FIG. 14.— Estimation of the most likely bias (*left*) and the confidence level (*right*) of the best-fit rotation amplitudes (Figures 13 and 15) for UCDs, blue GCs, and red GCs at  $R_{\text{av}} < 30'$ . In both the *left* and *right* panels, the black, blue and red colors correspond to results for the UCDs, blue GCs and red GCs respectively. In the *left* panel, curves of different colors correspond to the bias correction relation, as described in Section 8.2, for the three populations, and the *open squares* mark the best-fit rotation amplitudes for the real data sets. In the *right* panel, the open histograms represent the normalized distribution of best-fit rotation amplitudes for randomly shuffled samples, and the *filled* region of each histogram marks the probability  $p$  of obtaining a rotation amplitude greater than the best-fit value for the real data set just by chance, with the confidence level (CL) for the rotation being defined as  $1 - p$ .

pal axis” is thought to be the direction along which material flows into the cluster and forms galaxies, as seen in Cosmological  $N$ -body simulations (e.g. van Haarlem, Frenk & White 1997; Hopkins, Bahcall & Bode 2005; Faltenbacher et al. 2005).

## 9. ORBITAL ANISOTROPIES FROM JEANS ANALYSIS

### 9.1. Method

In this section we will infer the orbital anisotropies of UCDs and GCs based on the spherically symmetric Jeans equation

$$-n_r \frac{GM(<r)}{r^2} = \frac{d(n_r \sigma_r^2)}{dr} + 2 \frac{\beta_r}{r} n_r \sigma_r^2 \quad (8)$$

where  $M(<r)$  is the mass interior to the three-dimensional radius  $r$ .  $n_r$  and  $\sigma_r$  are respectively the volume number density and radial component of the velocity dispersion at radius  $r$  for a given tracer population, and  $\beta_r$  is the anisotropy parameter defined as  $1 - \sigma_t^2 / 2\sigma_r^2$ ,

with  $\sigma_t$  being the tangential components ( $\sigma_t^2 = \sigma_\theta^2 + \sigma_\phi^2$ ) of the velocity dispersion (Binney & Tremaine 2008).

In using Equation 8, we have assumed that the net rotation can be either ignored or simply folded into the velocity dispersion term. This approximation is reasonable given the fact that the overall rotation of our samples is not dynamically important ( $v_{\text{rot}}/\sigma_p \lesssim 0.4$ ). In addition, as mentioned previously, the M87 system is probably triaxial in shape, which would caution against a spherically symmetric Jeans analysis. However, as (at least) a first order approximation, it is definitely enlightening to do a comparative study of UCDs and GCs under the spherically symmetric assumption.

The anisotropy parameter  $\beta_r$  can be constrained if  $M(<r)$ ,  $n_r$ , and  $\sigma_r$  are known. For  $M(<r)$ , we adopt the most recent determination by Zhu et al. (2014) based on made-to-measure modeling (Syer & Tremaine 1996; Long & Mao 2010) of over 900 M87 GCs, which extend out to a projected radius of  $\sim 180 \text{ kpc}$ . The Zhu et al.

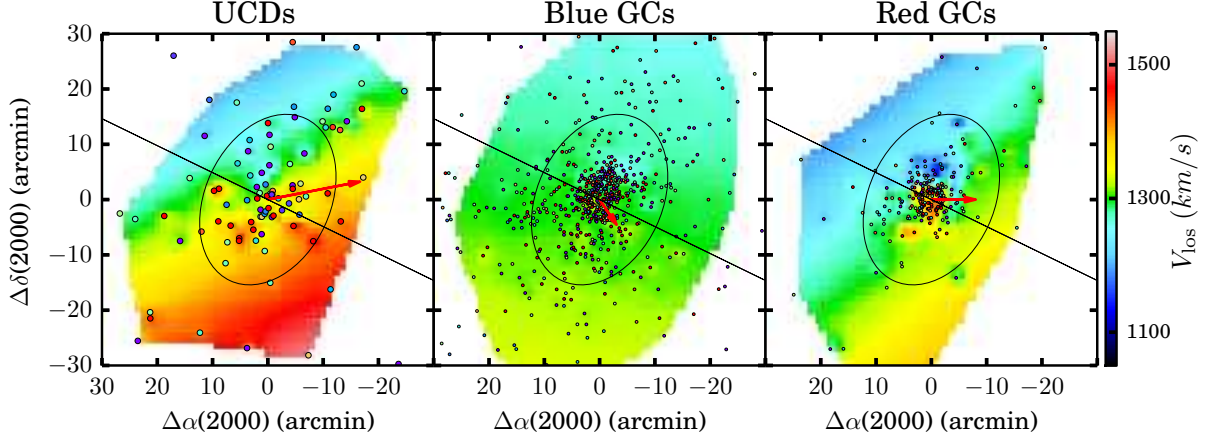


FIG. 15.— Spatial distribution of the UCDs (left), blue GCs (middle) and red GCs (right) are over plotted on their respective surface fitting (the color background) to the spatial distribution of line-of-sight velocities with the Kriging technique for the inner 30' of M87. The black ellipses represent the stellar isophotes of M87 at  $10R_e$ , and the black solid line marks the photometric minor axis of M87 in each panel. The red arrows, with the length being proportional to the rotation amplitude, mark the direction of rotation axis from our global kinematics fitting to the inner 30' (Figure 13). The global kinematics fitting, which is primarily driven by the inner regions that contain most of the data points, matches the central velocity field from Kriging surface fitting. Among the three populations, the blue GCs seem to have an overall velocity field more aligned with the photometric major axis than the other two populations. See the text for details.

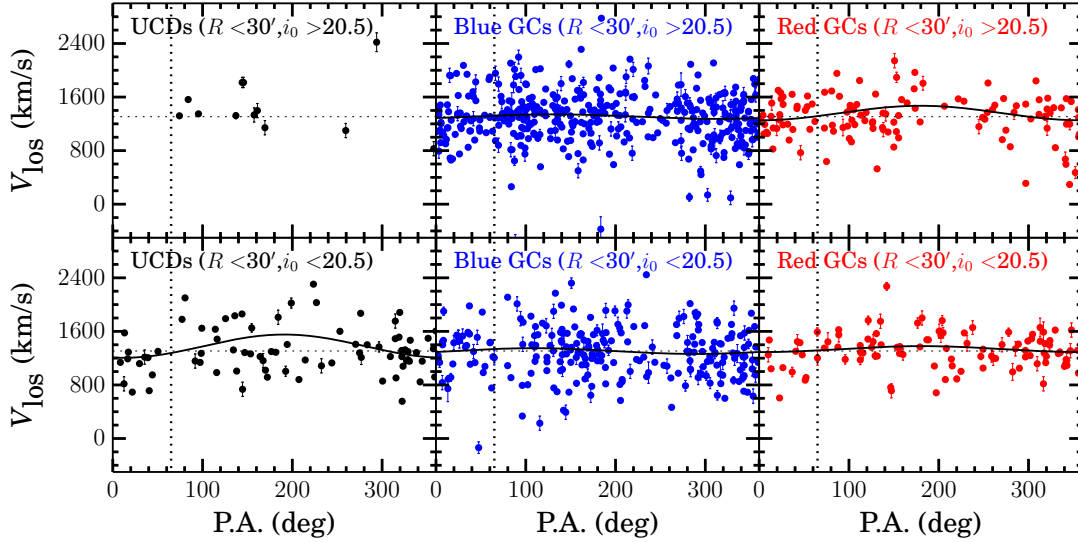


FIG. 16.— Radial velocity variations as a function of PA for the brighter (lower panels) and fainter (upper panels) subsamples of UCDs, blue GCs (middle), and Red GCs (right). Overlaid on the data in each panel is the best-fit sine curves. The horizontal dotted lines mark the systemic radial velocity of  $1307 \text{ km s}^{-1}$  of M87, and the vertical dotted lines mark PA of the photometric minor axis of M87.

(2014) mass profile is a combination of a stellar component and a spherical logarithmic dark matter halo model. The  $n_r$  profile is generally related to the surface number density profile  $N_R$  through the Abel integral equation. In particular, for deprojection of the Sérsic surface profile that was used to characterize  $N_R$  of the UCDs and GCs in this work (Table 1), we adopt the analytical approximation proposed by Prugniel & Simien (1997, Eq. B6; see also Mamon & Lokas 2005). In addition, treating the Jeans equation (8) as a first-order linear differential equation for  $n_r \sigma_r^2$ , one finds (See also Côté et al. 2001; Mamon & Lokas 2005)

$$\sigma_r^2 = -\frac{1}{n_r e^{[2 \int \frac{\beta_r}{t} dt]}} \int_r^\infty e^{[2 \int \frac{\beta_t}{t} dt]} n_t \frac{GM(< t)}{t^2} dt \quad (9)$$

The line-of-sight velocity dispersion  $\sigma_{\text{los},R}$  at projected

radius  $R$  is determined (e.g. Binney & Mamon 1982) as

$$\sigma_{\text{los},R}^2 = \frac{2}{N_R} \int_R^\infty n_r \sigma_r^2 (1 - \beta_r \frac{R^2}{r^2}) \frac{r}{\sqrt{r^2 - R^2}} dr \quad (10)$$

For the radial dependence of  $\beta_r$ , we adopt the following function form (first proposed by Mamon, Biviano & Boué 2013),

$$\beta_r = \beta_0 + (\beta_\infty - \beta_0) \frac{r}{r + r_\beta} \quad (11)$$

where  $\beta_0$ ,  $\beta_\infty$  and  $r_\beta$  are the three free parameters defining the radial profile. Specifically,  $\beta_0$  and  $\beta_\infty$  are the anisotropies at  $r = 0$  and  $\infty$  respectively, and  $r_\beta$  represents the scale radius of  $\beta_r$  profile. This function form of  $\beta_r$  allows for either a radially increasing or decreasing profile.

The GC (the blue plus red) anisotropy profile as determined by Zhu et al. (2014) shows a non-monotonic

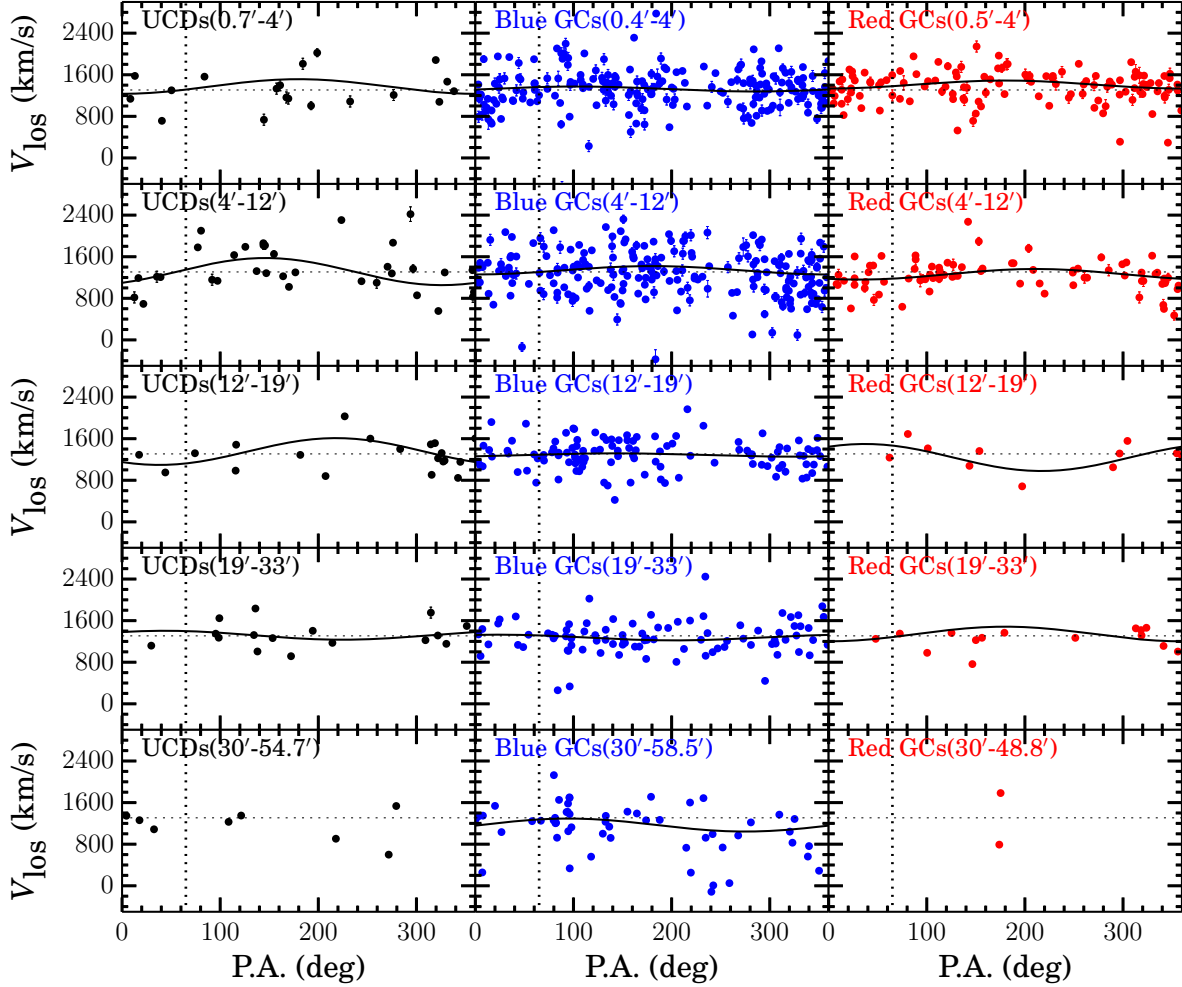


FIG. 17.— Radial velocity variations as a function of PA in five elliptical annuli for the full samples of UCDs (left), blue GCs (middle), and red GCs (right). The dotted lines mark the systemic radial velocity of  $1307 \text{ km s}^{-1}$  for M87. The five elliptical annuli plotted here are selected to be representative of the primary features exhibited in the radial profiles of kinematics shown in Figure 18.

behavior, in the sense that  $\beta_r$  gradually increases toward the intermediate radii ( $\sim 40 \text{ kpc}$ ) and then falls off in larger radii. Therefore, we also considered a two-part piecewise radial dependence of anisotropies by allowing the inner and outer radii to follow different profiles as defined by Equation 11, with the “transition” radius  $r_{\text{tr}}$  being left as a free parameter.

To constrain the radial anisotropy profiles for each of the different samples, we first created a library of model  $\sigma_{\text{los},R}$  profiles for each of them by allowing the free parameters that define the inner and outer anisotropy profiles to uniformly (linearly for  $\beta_0$ ,  $\beta_\infty$ , and  $r_{\text{tr}}$ , logarithmically for  $r_\beta$ ) vary. Then a maximum likelihood method was used to fit the models to the observed line-of-sight velocities as a function of projected radii. In particular, by assuming that the observed line-of-sight velocities  $v_i$  ( $\pm \Delta v_i$ ) at a given projected radius  $R$  follow a Gaussian distribution with  $\sigma_i^2 = (\Delta v_i)^2 + \sigma_{\text{los},R}^2$  and  $\mu = \sum_i (\frac{1}{\sigma_i^2} v_i) / \sum_i (\frac{1}{\sigma_i^2})$ , we calculated a joint probability (similar to Eq. 5 in form) of each model profile for a given population. The most probable model profile is taken as the fiducial one, and the 68% confidence intervals are determined by randomly resampling the real data sets, with  $\sim 10\%$  of data points being left out for each resample.

## 9.2. Results

The derived anisotropy profiles for the full samples of UCDs and GCs within the central  $35'$  of M87 are shown in Figure 20. Following Zhu et al. (2014), we reduced the weight of the data points (by increasing the uncertainties) that are located in the puzzlingly “hot” radius range from  $R_{\text{av}} = 4'$  to  $12'$  in the Jeans modeling. Since our Jeans analysis relies on the Zhu et al. mass profile, which was determined with made-to-measure modeling of nearly the same GC data set that is used in this work, we should obtain an anisotropy profile that is at least qualitatively consistent with Zhu et al. Comparing our Figure 20 to the Figure 12 of Zhu et al. (2014), one can see that, although being based on different methods, our anisotropy profile for the blue GCs, which dominate the spectroscopic samples of M87 GCs, is in reasonably good agreement with Zhu et al. within the uncertainties.

The UCD system has an anisotropy profile that becomes more radial with radius, with  $\beta_r$  being negative (tangentially-biased) within the inner  $\sim 20 - 40 \text{ kpc}$  and being positive (radially-biased) beyond. We note that a radially-biased orbital structure for UCDs at larger radii is in line with a peaky velocity distribution shown in Section 7. The blue GC system has a radially increasing  $\beta_r$  profile in the inner  $\sim 40 \text{ kpc}$  but a radially decreas-

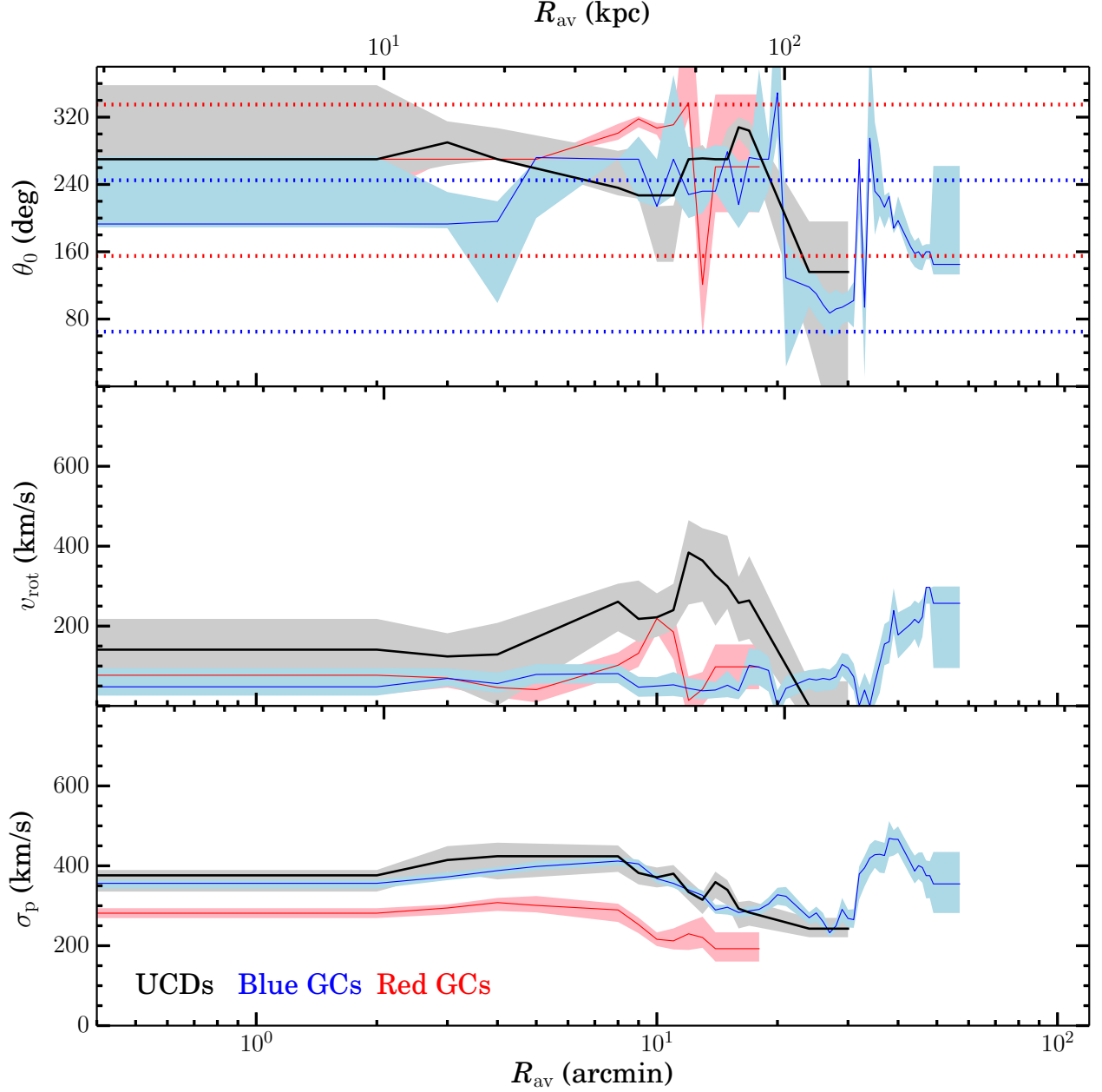


FIG. 18.— Radial variation of the best-fit kinematic parameters. The profiles were constructed with sliding bins of fixed radial widths, as in Figure 9. The red (blue) dotted horizontal lines in the top panel mark the photometric semi-major (semi-minor) axes. To be used in constructing the profiles, at least 19 data points should be available for the kinematics fitting in a given radial bin. The solid curves are the best-fit kinematics parameters, and the shaded regions correspond to the 68% confidence limits.

ing profile at larger radii. Among the three samples, the red GCs exhibit the largest radially-biased velocity dispersion tensor across the explored radius range, which may be surprising but nevertheless in line with their relatively large velocity kurtosis (Figure 10; Table 2). We note that, although being based on different mass models of M87, a highly radially-biased anisotropy ( $\beta \sim 0.8$  at  $\sim 150$  kpc) was also found in the outer stellar halo of M87 by Doherty et al. (2009) based on the integrated stellar absorption-line data at small radii and planetary nebulae (PNs; trace the stellar diffuse light, Coccato et al. 2009) kinematics at large radii ( $\lesssim 150$  kpc), and this is in agreement with our finding for red GCs. <sup>§</sup>

<sup>§</sup> Agnello et al. (2014) recently determined the anisotropies for

354 GCs within  $\sim 100$  kpc of M87, by dividing the GC system into three kinematically distinct subpopulations of different colors, i.e. blue, intermediate-color and red GCs, with intermediate GCs mostly being separated out from the classic red GCs. Agnello et al. found a mildly radially-biased anisotropy ( $\sim 0.3$ ) for their intermediate GCs and a slightly tangentially-biased anisotropy ( $\sim -0.2$ ) for their red GCs. Nevertheless, a tripartition of M87 GCs may be still oversimplified. As was shown by S11 (c.f. their Figure 8), there is a complex color dependence of velocity dispersion of the classic red GCs, in the sense that the “intermediate” red GCs have a significantly higher dispersion than both the “bluer” and “redder” red GCs. So, there may be at least three kinematically distinct subpopulations for the classic red GCs alone, and the red GC system has not completely mixed dynamically. A complete understanding of the dynamics of the red GCs would have to wait for larger samples of radial velocities across the M87 system, in order to explore the full color dependence of their dynamics.



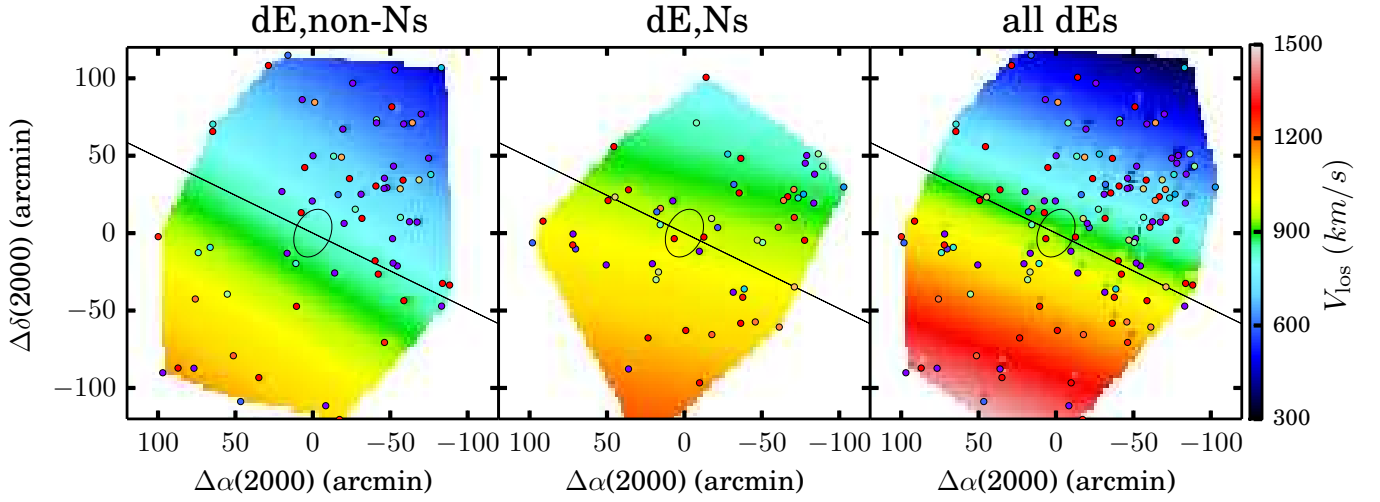


FIG. 19.— Spatial distribution of the non-nucleated dEs (*left*), nucleated dEs (*middle*) and all dEs (*right*) are over plotted on their respective color-coded surface fitting to the line-of-sight velocities with the Kriging technique for the inner 120' of M87. The *black ellipses* represent the stellar isophotes of M87 at  $10R_e$ , and the *black solid line* marks the photometric minor axis of M87 in each panel. Note that the direction of velocity gradients for both the nucleated and non-nucleated dEs roughly follows the photometric major axis of M87. When compared to the velocity fields shown in Figure 15, the dEs seem to be more aligned with the blue GCs than the UCDs and red GCs.

TABLE 2  
KINEMATICS OF THE FULL SAMPLES

$R_{av}$ (arcmin) (1)	$N$ (2)	$v_{sys}$ (km s <sup>-1</sup> ) (3)	$\theta_0$ (deg) (4)	$v_{rot}$ (km s <sup>-1</sup> ) (5)	$v_{rot, bias-corr}$ (km s <sup>-1</sup> ) (6)	CL (7)	$\sigma_p$ (km s <sup>-1</sup> ) (8)	$v_{rms}$ (km s <sup>-1</sup> ) (9)	$G_2$ (10)	$T$ (11)
UCDs										
0.7'–30'	89	1385 <sup>+31</sup> <sub>-54</sub>	281 <sup>+13</sup> <sub>-14</sub>	154 <sup>+39</sup> <sub>-44</sub>	144	98%	344 <sup>+15</sup> <sub>-18</sub>	355 <sup>+16</sup> <sub>-19</sub>	-0.2 <sup>+0.2</sup> <sub>-0.2</sub>	0.8 <sup>+0.1</sup> <sub>-0.4</sub>
0.7'–4'	19	1374 <sup>+69</sup> <sub>-68</sub>	270 <sup>+90</sup> <sub>-33</sub>	141 <sup>+82</sup> <sub>-79</sub>	0–10	62%	376 <sup>+13</sup> <sub>-57</sub>	392 <sup>+23</sup> <sub>-61</sub>	-0.1 <sup>+0.6</sup> <sub>-0.4</sub>	0.1 <sup>+0.4</sup> <sub>-0.2</sub>
4'–12'	34	1314 <sup>+44</sup> <sub>-38</sub>	236 <sup>+63</sup> <sub>-26</sub>	241 <sup>+50</sup> <sub>-62</sub>	240	99%	424 <sup>+36</sup> <sub>-53</sub>	453 <sup>+32</sup> <sub>-35</sub>	-0.1 <sup>+0.4</sup> <sub>-0.3</sub>	0.1 <sup>+0.3</sup> <sub>-0.3</sub>
12'–30'	36	1352 <sup>+37</sup> <sub>-38</sub>	304 <sup>+9</sup> <sub>-21</sub>	150 <sup>+41</sup> <sub>-62</sub>	130	87%	262 <sup>+25</sup> <sub>-24</sub>	262 <sup>+16</sup> <sub>-23</sub>	-0.3 <sup>+0.3</sup> <sub>-0.3</sub>	0.4 <sup>+0.2</sup> <sub>-0.3</sub>
30'–60'	8	...	...	...	...	...	...	...	...	...
Blue GCs										
0.4'–30'	615	1306 <sup>+21</sup> <sub>-19</sub>	214 <sup>+69</sup> <sub>-11</sub>	36 <sup>+28</sup> <sub>-14</sub>	30	73%	357 <sup>+5</sup> <sub>-8</sub>	357 <sup>+5</sup> <sub>-7</sub>	-0.2 <sup>+0.1</sup> <sub>-0.1</sub>	0.1 <sup>+0.1</sup> <sub>-0.1</sub>
0.4'–4'	207	1326 <sup>+31</sup> <sub>-17</sub>	193 <sup>+83</sup> <sub>-91</sub>	48 <sup>+45</sup> <sub>-21</sub>	20	55%	354 <sup>+9</sup> <sub>-13</sub>	354 <sup>+11</sup> <sub>-11</sub>	-0.2 <sup>+0.1</sup> <sub>-0.1</sub>	0.1 <sup>+0.1</sup> <sub>-0.1</sub>
4'–12'	219	1339 <sup>+18</sup> <sub>-26</sub>	270 <sup>+15</sup> <sub>-35</sub>	81 <sup>+23</sup> <sub>-24</sub>	72	84%	412 <sup>+10</sup> <sub>-11</sub>	415 <sup>+7</sup> <sub>-14</sub>	-0.7 <sup>+0.1</sup> <sub>-0.1</sub>	0.0 <sup>+0.1</sup> <sub>-0.1</sub>
12'–30'	189	1282 <sup>+12</sup> <sub>-13</sub>	161 <sup>+52</sup> <sub>-58</sub>	26 <sup>+17</sup> <sub>-27</sub>	0–20	22%	267 <sup>+11</sup> <sub>-9</sub>	267 <sup>+9</sup> <sub>-7</sub>	-0.3 <sup>+0.1</sup> <sub>-0.1</sub>	0.2 <sup>+0.1</sup> <sub>-0.1</sub>
30'–60'	54	1168 <sup>+32</sup> <sub>-30</sub>	185 <sup>+44</sup> <sub>-19</sub>	125 <sup>+41</sup> <sub>-46</sub>	91	80%	438 <sup>+33</sup> <sub>-27</sub>	465 <sup>+28</sup> <sub>-41</sub>	...	...
Red GCs										
0.5'–30'	226	1341 <sup>+15</sup> <sub>-15</sub>	270 <sup>+21</sup> <sub>-10</sub>	62 <sup>+22</sup> <sub>-19</sub>	61	87%	268 <sup>+10</sup> <sub>-8</sub>	277 <sup>+6</sup> <sub>-12</sub>	0.2 <sup>+0.1</sup> <sub>-0.1</sub>	0.1 <sup>+0.1</sup> <sub>-0.1</sub>
0.5'–4'	122	1404 <sup>+24</sup> <sub>-29</sub>	270 <sup>+67</sup> <sub>-41</sub>	77 <sup>+30</sup> <sub>-48</sub>	71	80%	272 <sup>+8</sup> <sub>-14</sub>	272 <sup>+10</sup> <sub>-11</sub>	-0.2 <sup>+0.2</sup> <sub>-0.1</sub>	-0.1 <sup>+0.2</sup> <sub>-0.1</sub>
4'–12'	78	1261 <sup>+21</sup> <sub>-19</sub>	301 <sup>+9</sup> <sub>-9</sub>	102 <sup>+34</sup> <sub>-28</sub>	80	86%	284 <sup>+15</sup> <sub>-30</sub>	284 <sup>+17</sup> <sub>-19</sub>	0.8 <sup>+0.4</sup> <sub>-0.3</sub>	0.2 <sup>+0.2</sup> <sub>-0.2</sub>
12'–30'	26	1242 <sup>+36</sup> <sub>-26</sub>	105 <sup>+18</sup> <sub>-36</sub>	106 <sup>+39</sup> <sub>-50</sub>	41	67%	216 <sup>+17</sup> <sub>-18</sub>	228 <sup>+20</sup> <sub>-38</sub>	1.0 <sup>+0.7</sup> <sub>-0.6</sub>	0.4 <sup>+0.5</sup> <sub>-0.4</sub>
30'–60'	3	...	...	...	...	...	...	...	...	...

NOTE. — (1) The range of geometric galactocentric distances from the center of M87. (2) Number of data points used in the kinematics modeling. (3) The best-fit systematic velocity. (4) The best-fit azimuthal angle of the rotation axis, east of north. (5) The best-fit rotation amplitude. (6) The bias-corrected rotation amplitude. (7) The confidence level of the best-fit rotation. (8) The rotation-subtracted velocity dispersion. (9) The biweight root-mean-square velocity. (10) Standard kurtosis  $G_2$  of the velocity distribution. (11) The  $T$  parameter proposed by Moors (1988). As a quantile-based alternative for the standard kurtosis,  $T$  is an increasing function of  $G_2$ . See the Appendix for definition of  $T$ .



TABLE 3  
KINEMATICS OF THE SUBSAMPLES WITH  $i_0 < 20.5$

$R_{\text{av}}$ (arcmin) (1)	$N$ (2)	$v_{\text{sys}}$ (km s $^{-1}$ ) (3)	$\theta_0$ (deg) (4)	$v_{\text{rot}}$ (km s $^{-1}$ ) (5)	$v_{\text{rot, bias-corr}}$ (km s $^{-1}$ ) (6)	CL (7)	$\sigma_p$ (km s $^{-1}$ ) (8)	$v_{\text{rms}}$ (km s $^{-1}$ ) (9)	$G_2$ (10)	$T$ (11)
UCDs										
0.7'–30'	78	1379 $^{+58}_{-57}$	281 $^{+10}_{-24}$	174 $^{+64}_{-70}$	154	98%	352 $^{+11}_{-20}$	360 $^{+14}_{-23}$	-0.2 $^{+0.2}_{-0.2}$	0.7 $^{+0.1}_{-0.5}$
0.7'–4'	15	1272 $^{+127}_{-125}$	358 $^{+54}_{-66}$	238 $^{+135}_{-107}$	141	63%	371 $^{+16}_{-39}$	437 $^{+12}_{-80}$	-0.4 $^{+0.7}_{-0.5}$	0.4 $^{+0.4}_{-0.5}$
4'–12'	29	1309 $^{+170}_{-86}$	237 $^{+73}_{-69}$	244 $^{+141}_{-102}$	240	89%	388 $^{+32}_{-43}$	429 $^{+25}_{-39}$	-0.2 $^{+0.4}_{-0.4}$	0.3 $^{+0.4}_{-0.4}$
12'–30'	34	1342 $^{+66}_{-53}$	309 $^{+17}_{-36}$	151 $^{+86}_{-104}$	120	84%	282 $^{+29}_{-21}$	293 $^{+19}_{-25}$	0.1 $^{+0.5}_{-0.5}$	0.3 $^{+0.2}_{-0.3}$
30'–60'	8	...	...	...	...	...	...	...	...	...
Blue GCs										
0.4'–30'	242	1306 $^{+26}_{-23}$	199 $^{+47}_{-103}$	43 $^{+33}_{-34}$	11	49%	360 $^{+9}_{-11}$	360 $^{+8}_{-10}$	-0.5 $^{+0.1}_{-0.1}$	0.0 $^{+0.1}_{-0.1}$
0.4'–4'	67	1336 $^{+46}_{-45}$	188 $^{+54}_{-74}$	38 $^{+58}_{-50}$	0	17%	355 $^{+16}_{-15}$	357 $^{+12}_{-17}$	-0.7 $^{+0.2}_{-0.1}$	0.0 $^{+0.2}_{-0.2}$
4'–12'	95	1321 $^{+48}_{-42}$	203 $^{+73}_{-56}$	152 $^{+59}_{-67}$	140	90%	439 $^{+16}_{-19}$	446 $^{+13}_{-10}$	-0.7 $^{+0.2}_{-0.1}$	0.0 $^{+0.1}_{-0.2}$
12'–30'	80	1285 $^{+30}_{-34}$	40 $^{+56}_{-48}$	62 $^{+43}_{-37}$	26	51%	265 $^{+12}_{-12}$	269 $^{+19}_{-14}$	-0.3 $^{+0.2}_{-0.2}$	-0.2 $^{+0.2}_{-0.1}$
30'–60'	22	1014 $^{+77}_{-45}$	270 $^{+64}_{-16}$	0 $^{+125}_{-105}$	0	80%	381 $^{+41}_{-31}$	381 $^{+42}_{-33}$	...	...
Red GCs										
0.5'–30'	102	1335 $^{+28}_{-29}$	271 $^{+9}_{-37}$	45 $^{+43}_{-38}$	0	44%	264 $^{+16}_{-14}$	269 $^{+11}_{-15}$	0.2 $^{+0.2}_{-0.2}$	0.1 $^{+0.2}_{-0.1}$
0.5'–4'	39	1402 $^{+41}_{-46}$	270 $^{+86}_{-87}$	92 $^{+56}_{-55}$	50	66%	249 $^{+17}_{-19}$	249 $^{+12}_{-18}$	-0.9 $^{+0.2}_{-0.2}$	-0.2 $^{+0.1}_{-0.2}$
4'–12'	47	1296 $^{+56}_{-47}$	306 $^{+10}_{-10}$	59 $^{+90}_{-64}$	0	35%	261 $^{+16}_{-23}$	270 $^{+12}_{-27}$	0.6 $^{+0.4}_{-0.5}$	0.0 $^{+0.2}_{-0.2}$
12'–30'	16	1247 $^{+61}_{-65}$	101 $^{+30}_{-70}$	35 $^{+48}_{-34}$	0	10%	173 $^{+35}_{-52}$	175 $^{+26}_{-41}$	1.2 $^{+0.6}_{-0.8}$	1.1 $^{+0.6}_{-0.6}$
30'–60'	0	...	...	...	...	...	...	...	...	...

NOTE. — (1) The range of geometric galactocentric distances from the center of M87. (2) Number of data points used in the kinematics modeling. (3) The best-fit systematic velocity. (4) The best-fit azimuthal angle of the rotation axis, east of north. (5) The best-fit rotation amplitude. (6) The bias-corrected rotation amplitude. (7) The confidence level of the best-fit rotation. (8) The rotation-subtracted velocity dispersion. (9) The biweight root-mean-square velocity. (10) Standard kurtosis  $G_2$  of the velocity distribution. (11) The  $T$  parameter proposed by Moors (1988). As a quantile-based alternative for the standard kurtosis,  $T$  is an increasing function of  $G_2$ . See the Appendix for definition of  $T$ .

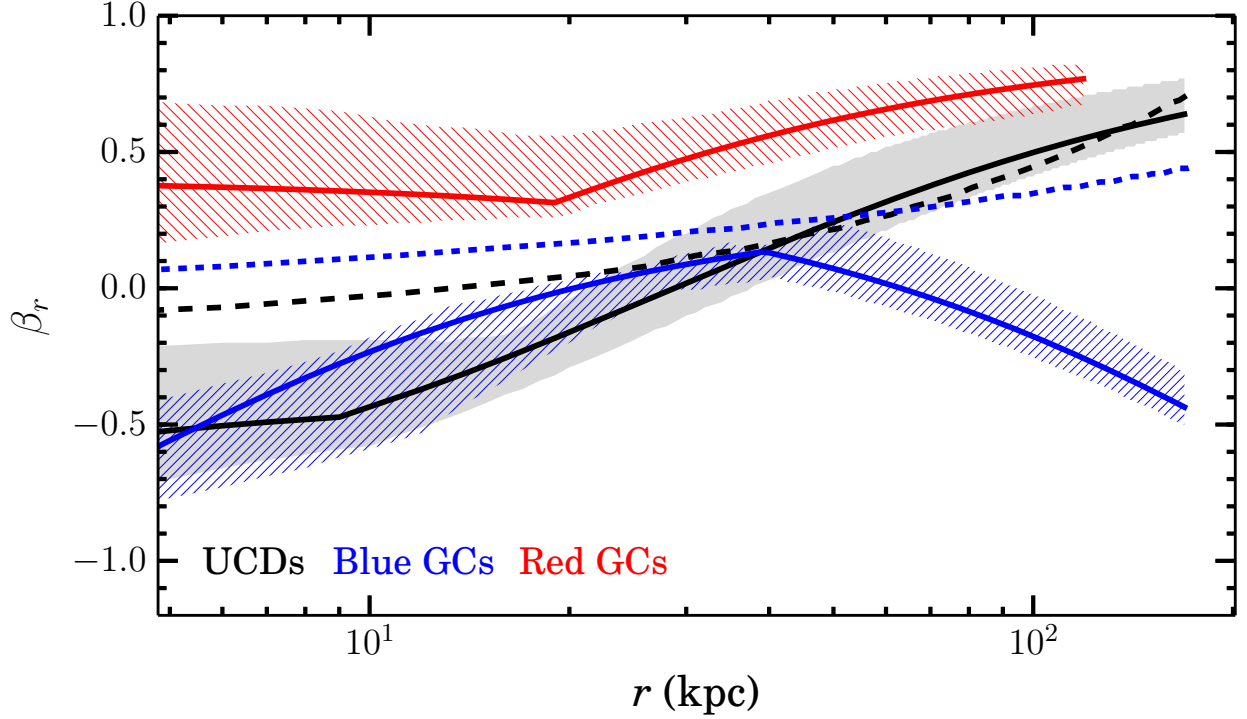


FIG. 20.— Variation of the anisotropy parameters as a function of the 3D radius. The profiles for UCDs, blue GCs, and red GCs are represented as black, blue, and red solid curves respectively. Following the same color code, the hatched regions of different styles mark the 68% confidence intervals for blue GCs, and red GCs. The grey shaded region marks the 68% confidence interval for the UCDs. The short dashed curves (black for UCDs, blue for blue GCs) represent the anisotropy profiles predicted by a universal relation between the number density slope and  $\beta$  for relic high- $\sigma$  density peaks as found in cosmological simulations by Diemand et al. (2005).

TABLE 4  
KINEMATICS OF THE SUBSAMPLES WITH  $i_0 > 20.5$

$R_{av}$ (arcmin) (1)	$N$ (2)	$v_{sys}$ (km s $^{-1}$ ) (3)	$\theta_0$ (deg) (4)	$v_{rot}$ (km s $^{-1}$ ) (5)	$v_{rot,bias-corr}$ (km s $^{-1}$ ) (6)	CL (7)	$\sigma_p$ (km s $^{-1}$ ) (8)	$v_{rms}$ (km s $^{-1}$ ) (9)	$G_2$ (10)	$T$ (11)
UCDs										
0.7'–30'	11	...	...	...	...	...	...	$406^{+114}_{-93}$	...	...
0.7'–4'	4	...	...	...	...	...	...	...	...	...
4'–12'	5	...	...	...	...	...	...	...	...	...
12'–30'	2	...	...	...	...	...	...	...	...	...
30'–60'	0	...	...	...	...	...	...	...	...	...
Blue GCs										
0.4'–30'	373	$1308^{+25}_{-21}$	$220^{+31}_{-106}$	$34^{+34}_{-27}$	11	51%	$352^{+9}_{-8}$	$352^{+8}_{-8}$	$-0.1^{+0.1}_{-0.1}$	$0.1^{+0.1}_{-0.1}$
0.4'–4'	140	$1344^{+35}_{-33}$	$232^{+75}_{-85}$	$71^{+42}_{-37}$	55	71%	$357^{+15}_{-15}$	$361^{+15}_{-14}$	$0.2^{+0.2}_{-0.2}$	$0.2^{+0.1}_{-0.1}$
4'–12'	124	$1352^{+40}_{-38}$	$270^{+76}_{-76}$	$87^{+51}_{-51}$	61	77%	$421^{+19}_{-19}$	$421^{+19}_{-14}$	$0.2^{+0.2}_{-0.2}$	$0.1^{+0.1}_{-0.1}$
12'–30'	109	$1267^{+30}_{-29}$	$216^{+71}_{-40}$	$44^{+37}_{-33}$	6	38%	$269^{+14}_{-13}$	$269^{+10}_{-12}$	$-0.1^{+0.2}_{-0.2}$	$0.4^{+0.1}_{-0.2}$
30'–60'	32	$1253^{+53}_{-55}$	$136^{+50}_{-23}$	$139^{+84}_{-105}$	90	73%	$443^{+75}_{-52}$	$487^{+53}_{-76}$	...	...
Red GCs										
0.5'–30'	124	$1361^{+37}_{-39}$	$270^{+62}_{-52}$	$109^{+51}_{-49}$	108	94%	$310^{+19}_{-13}$	$319^{+15}_{-16}$	$1.1^{+0.3}_{-0.3}$	$0.0^{+0.1}_{-0.1}$
0.5'–4'	83	$1358^{+52}_{-45}$	$222^{+39}_{-100}$	$47^{+60}_{-51}$	0	27%	$320^{+24}_{-20}$	$329^{+17}_{-25}$	$1.7^{+0.4}_{-0.5}$	$0.2^{+0.1}_{-0.2}$
4'–12'	31	$1231^{+45}_{-41}$	$293^{+25}_{-20}$	$12^{+84}_{-12}$	0	4%	$297^{+31}_{-32}$	$299^{+35}_{-30}$	$0.6^{+0.8}_{-0.6}$	$1.2^{+0.4}_{-0.7}$
12'–30'	10	...	...	...	...	...	...	$155^{+14}_{-22}$	...	...
30'–60'	3	...	...	...	...	...	...	...	...	...

NOTE. — (1) The range of geometric galactocentric distances from the center of M87. (2) Number of data points used in the kinematics modeling. (3) The best-fit systematic velocity. (4) The best-fit azimuthal angle of the rotation axis, east of north. (5) The best-fit rotation amplitude. (6) The bias-corrected rotation amplitude. (7) The confidence level of the best-fit rotation. (8) The rotation-subtracted velocity dispersion. (9) The biweight root-mean-square velocity. (10) Standard kurtosis  $G_2$  of the velocity distribution. (11) The  $T$  parameter proposed by Moors (1988). As a quantile-based alternative for the standard kurtosis,  $T$  is an increasing function of  $G_2$ . See the Appendix for definition of  $T$ .

### 9.3. Interpretation

The different orbital anisotropies of the different populations may be attributed to either their different origin or different orbital evolutionary histories. Our size-defined UCDs have at least an order of magnitude lower average density than GCs of similar luminosity, which means that UCDs are subject to a stronger tidal influence when approaching small galactocentric distances. In addition, at a given average orbital radius, objects with more radially-biased orbits can plunge deeper into the central regions of their host, and thus are prone to stronger tidal disruption. Recent simulations (Pfeffer & Baumgardt 2013) suggest that UCD-sized clusters can be converted, via a continuous tidal stripping of their envelope, into GC-sized objects at small galactocentric distances.

#### 9.3.1. Depletion of Radial Orbits of UCDs at Small Galactocentric Distances

The finding that UCDs in the central  $\sim 40$  kpc are depleted of radial orbits may be partly attributed to a stronger tidal influence at smaller galactocentric distances. To be quantitative, the Jacobi radius  $r_J$  of a stellar cluster moving in the tidal field of its host galaxy is determined by its galactocentric distance  $r_{gal}$ , the galaxy mass  $M_{gal}$  interior to  $r_{gal}$  and the cluster mass  $m$ . Specifically,  $r_J = r_{gal}(m/2M_{gal})^{1/3}$  (von Hoerner 1957; Innanen et al. 1983; Bertin & Varri 2008; Renaud et al. 2011; Webb et al. 2013). Based on this basic tidal theory and the Zhu et al. mass profile of M87, we estimated the ratio

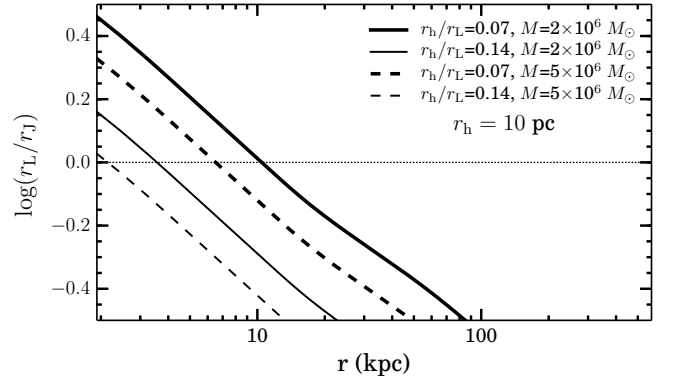


FIG. 21.— Radial variation of the ratio of limiting radius to Jacobi radius for M87 UCDs which have projected half-mass radii  $r_h = 10$  pc and  $M = 2 \times 10^6 M_\odot$  (solid curves) or  $5 \times 10^6 M_\odot$  (dashed curves). The thick and thin curves represent results respectively for  $r_h/r_L = 0.07$  and  $0.14$ , which straddle the range of  $r_h/r_L$  typical of the Galactic GCs based on King (1966) model fitting (McLaughlin & van der Marel 2005). The UCDs with  $\log(r_L/r_J) > 0$  were tidally over-filling, and thus should have been tidally truncated below 10 pc in  $r_h$ .

of limiting radius  $r_L$  to  $r_J$  as a function of galactocentric distances for M87 UCDs ( $m = 2 \times 10^6 M_\odot$  or  $5 \times 10^6 M_\odot$ ) with projected half-mass radius  $r_h = 10$  pc (Figure 21).  $r_L$  ideally represents the radius beyond which the stellar density of a cluster is zero, but in practice  $r_L$  is an extrapolated radius from either King or other model profile fitting (e.g. Harris 1996). In plotting Figure 21, we considered two different ratios of  $r_h/r_L$ , namely, 0.07 and 0.14, which cover the typical range for the Galactic

GCs based on King (1966) model fitting (McLaughlin & van der Marel 2005).

From Figure 21, it can be seen that the limiting radii are comparable to or greater than the Jacobi radii (tidally over-filling) at galactocentric distances  $\lesssim 10$  kpc for typical M87 UCDs if  $r_h/r_L \lesssim 0.07$ . Previous King profile fitting to some Virgo UCDs with the high-quality HST imaging data suggests that they have  $r_h/r_L < 0.1$  (e.g. Evstigneeva et al. 2007). It is thus quite plausible that many UCDs with  $r_h > 10$  pc at small galactocentric distances have been tidally truncated into GC-sized objects with  $r_h < 10$  pc, and this tidal transformation should be especially efficient for UCDs on plunging orbits at a given average galactocentric distance. Accordingly, UCDs that survives at smaller galactocentric distances are expected to have less radially-biased orbital structure, in line with our finding of an anisotropy profile that increases with radius for UCDs.

### 9.3.2. Different Assembly Histories of UCD and blue GC Systems

Although the tidal transformation effect discussed above should have been playing some role, it is not necessarily the sole or even dominant mechanism in shaping the present-day anisotropy profile of our size-defined UCDs. It is possible that the progenitors of many UCDs at smaller galactocentric distances have been primarily accreted from less radially-biased orbits.

In a  $\Lambda$ CDM Universe, a more radially-biased orbital structure for the outer stellar halos of early type galaxies seems to be a general outcome from a hierarchical structure formation (e.g. Dekel et al. 2005; Diemand et al. 2005; Hansen & Moore 2006; Abadi, Navarro & Steinmetz 2006). It has been conjectured that old halo populations, such as the metal-poor (blue) GCs, might form primarily in small dark matter halos that collapsed from high- $\sigma$  ( $> 2.5\sigma$ ; Diemand et al. 2005) peaks of the primordial density field at  $z > 10$  (e.g. Moore et al. 2006; Boley et al. 2009; Moran et al. 2014; see also a review by Brodie & Strader 2006). One interesting finding from the  $N$ -body cosmological simulation of Diemand et al. (2005) is the existence of a universal relation between the present-day density profile slope  $d \ln n / d \ln r$  and the anisotropy for the relic high- $\sigma$  peaks, and this relation is not sensitive to the detailed assembly histories. In particular, Diemand et al. (2005) found:  $\beta \simeq -0.23(1.2 + d \ln n / d \ln r)$ . By deprojecting the surface number density profiles presented in Section 5.4 under the assumption of a spherically symmetric geometry, we obtained the  $\beta$  profiles for M87 UCDs and blue GCs as expected by the above relation. The profiles are overplotted in Figure 20 as dashed lines.

Although being more negative in the innermost part, the  $\beta_r$  profile of UCDs determined from Jeans analysis is more or less consistent with the Diemand et al. predication within  $2\sigma$  uncertainties. As discussed above, the significantly tangentially-biased orbital structure of UCDs at small radii can be partly attributed to a strong tidal transformation. The derived  $\beta_r$  profile of the blue GCs exhibit large deviation from the Diemand et al. prediction. The finding that the blue GCs are tangentially-biased, rather than being radially-biased, at large radii

may indicate<sup>¶</sup> that the blue GC system in the outer halo of M87 has not yet established an equilibrium state and is still in an early and active stage of assembly, presumably through a continuous accretion of surrounding dwarf galaxies (e.g. Côté, Marzke & West 1998). Agnello et al. (2014) invoked the scenario of adiabatic contraction of the dark matter halo to explain the enhancement of tangentially-biased orbits of blue GCs of M87 at large radii, and this mechanism works when accretion of satellite galaxies happens on sufficiently slow time scales (Goodman & Binney 1984).

The agreement between the present-day radial anisotropy profile of UCDs and that predicted by cosmological simulations does not tell us the detailed accretion process of the UCD progenitors. Our finding that UCDs have radially-biased orbital structure at large galactocentric distances is in line with prediction of the “tidal threshing” scenario where UCDs were primarily tidally stripped dE nuclei (e.g. Bekki et al. 2003; Goerdt et al. 2008; Pfeffer & Baumgardt 2013), although the primary progenitor galaxies of UCDs do not necessarily resemble the present-day surviving dEs. Previous simulations suggest that, to be tidally-threshed to a naked nucleus, a dE,N galaxy has to be on a highly radially-biased orbit in order to plunge deep into the central potential. If tidal threshing is indeed the dominant channel for forming UCDs, our finding suggests that UCDs might be preferentially but not exclusively accreted from plunging orbits. Indeed, previous simulations (e.g. Gill et al. 2004; Smith et al. 2013) suggest that, at small galactocentric distances, satellite galaxies on circular orbits may also be tidally disrupted.

## 10. SUMMARY AND DISCUSSION

We have compiled a sample of 97 spectroscopically confirmed UCDs associated with the central cD galaxy of the Virgo cluster – M87 (NGC 4486). The UCDs are defined to have  $10 \lesssim r_h \lesssim 100$  pc. 89% of our sample have  $i_0 < 20.5$  mag ( $M_g < -10.6$ ), corresponding to a stellar mass of  $\sim 2 \times 10^6 M_\odot$ . In addition, 92% of the UCDs have colors as blue as the classic blue GCs. Throughout this paper, we compared the distribution and dynamics of UCDs to that of M87 GCs. The primary results of this paper are summarized as follows.

1. The M87 UCD system has a surface number density profile that is shallower than the blue GCs in the inner  $\sim 15'$  ( $\sim 70$  kpc) and as steep as the red GCs at larger radii. In addition, the UCDs follow a radial velocity dispersion profile more similar to that of the blue rather than the red GCs.
2. Overall, the UCD system exhibits a significantly stronger rotation than the GC system. No significant rotation was found for either the bright ( $M_g < -10.6$ ) or faint ( $M_g > -10.6$ ) blue GCs. Although subject to relatively large uncertainties, the velocity field of dE galaxies surrounding M87 seems to be more aligned with that of the blue GCs rather than the UCDs.

<sup>¶</sup> Another possibility could be that the outer halo mass of M87 may be somehow underestimated, which would artificially lead to a lower  $\beta$  due to the mass-anisotropy degeneracy.

3. The velocity distribution of UCDs is characterized by a sharper peak and marginally lighter tails compared to a Gaussian distribution. This is in general agreement with results from Jeans analysis, namely, anisotropy of the velocity dispersion tensor of UCDs gradually increases from being tangentially-biased at inner radii to being radially-biased at larger radii. Overall, the GCs have velocity distribution similar to a Gaussian, with the blue GCs being slightly platykurtic and the red GCs being slightly leptokurtic. In addition, the bright blue GCs have velocity kurtosis systematically higher than the faint ones across the full range of galactocentric distances, indicating that the bright ones are more tangentially-biased than the faint ones.
4. The M87 UCD system has an orbital anisotropy profile that gradually increases with galactocentric distances, with UCDs within  $\sim 40$  kpc being tangentially-biased while being radially-biased outward. In contrast to UCDs, the blue GCs beyond  $\sim 40$  kpc become gradually more tangentially-biased toward larger radii. The tangentially-biased anisotropy of UCDs in the inner region may be partly attributed to a continuous tidal transformation of UCD-sized objects on plunging orbits to GC-sized clusters.

Above all, our analysis suggests that the M87 UCDs are dynamically distinct from GCs. Other evidence against UCDs being the most luminous and extended tails of normal GCs include their different Fundamental-Plane relation (e.g. luminosity vs. internal velocity dispersion, Chilingarian et al. 2011). Our finding that UCDs have radially-biased orbital structure at large galactocentric distances is in general agreement with the “tidal threshing” scenario that UCDs are primarily tidally stripped dE nuclei. In an accompanying paper, Liu et al. (2015) find that M87 UCDs at smaller galactocentric distances tend to have less prominent stellar envelopes than those lying at larger distances, providing direct evidence for tidal stripping. Moreover, previous studies (e.g. Paudel et al. 2010; Chilingarian et al. 2011; Francis et al. 2012) suggests that Virgo UCDs have metallicities that are high for their luminosity according to the metallicity-luminosity relation defined by early-type galaxies, which is naturally expected for the “tidally threshed dwarf galaxy” scenario.

In the context of  $\Lambda$ CDM hierarchical structure formation, as a more centrally confined population, UCDs might originate from rarer density peaks in the primordial density field than the more spatially distributed dwarf galaxies that have been presumably the main contributor of blue GCs to the outer halo of M87, and those rarer systems should collapse and fall into the central potential earlier. It is well known that the dE,N galaxies are strongly centrally clustered in galaxy clusters as compared to the non-nucleated dEs (e.g. van den Bergh

1986; Ferguson & Sandage 1989; Lisker et al. 2007). The distinct dynamical property of the UCD system might owe its origin to an earlier accretion of the progenitors of UCDs, and the present-day surviving dE,Ns do not necessarily resemble the primary UCD progenitors. In fact, most UCDs are found to be significantly older, more metal-poor and have super-solar alpha-element abundances compared to the majority of present-day dE nuclei. Future spectroscopic stellar population analysis of large sample of M87 UCDs will be invaluable in further shedding light on the difference between the UCDs, blue GCs and dE nuclei.

HXZ acknowledges support from China Postdoctoral Science Foundation under Grant No. 552101480582. HXZ also acknowledges support from CAS-CONICYT Postdoctoral Fellowship, administered by the Chinese Academy of Sciences South America Center for Astronomy (CASSACA). EWP acknowledges support from the National Natural Science Foundation of China under Grant No. 11173003, and from the Strategic Priority Research Program, “The Emergence of Cosmological Structures”, of the Chinese Academy of Sciences, Grant No. XDB09000105. EWP thanks the staff of the MMT and AAT observatories for their unfailingly professional support of the spectroscopic observations presented in this paper. CL acknowledges support from the National Natural Science Foundation of China (Grant No. 11203017 and 11125313).

This work is based on observations obtained with MegaPrime/MegaCam, a joint project of CFHT and CEA/DAPNIA, at the CanadaFranceHawaii Telescope (CFHT) which is operated by the National Research Council (NRC) of Canada, the Institut National des Sciences de l’Univers of the Centre National de la Recherche Scientifique (CNRS) of France and the University of Hawaii.

This research used the facilities of the Canadian Astronomy Data Centre operated by the National Research Council of Canada with the support of the Canadian Space Agency. The authors further acknowledge use of the NASA/IPAC Extragalactic Database (NED), which is operated by the Jet Propulsion Laboratory, California Institute of Technology, under contract with the National Aeronautics and Space Administration, and the HyperLeda database (<http://leda.univ-lyon1.fr>).

Observations reported here were obtained at the MMT Observatory, a joint facility of the University of Arizona and the Smithsonian Institution. MMT telescope time was granted, in part, by NOAO, through the Telescope System Instrumentation Program (TSIP). TSIP is funded by NSF. Data presented in this paper were obtained at the Anglo-Australian Telescope, which is operated by the Australian Astronomical Observatory.

*Facilities:* CFHT, AAT/AAOmega, MMT/Hectospec

## REFERENCES

- Ashman, K. M., & Zepf, S. E. 1992, *ApJ*, 384, 50  
 Abadi, M. G., Navarro, J. F., & Steinmetz, M. 2006, *MNRAS*, 365, 747  
 Agnello, A., Evans, N. W., Romanowsky, A. J., & Brodie, J. P. 2014, *MNRAS*, 442, 3299  
 Arnold, J. A., Romanowsky, A. J., Brodie, J. P. et al. 2014, *ApJ*, 791, 80  
 Bohringer, H., Briel, U. G., Schwarz, R. A., Voges, W., Hartner, G., & Trumpler, J. 1994, *Nature*, 368, 828

- Baumgardt, H., Parmentier, G., Gieles, M., & Vesperini, E. 2010, *MNRAS*, 401, 1832
- Bekki, K., Couch, W. J., Drinkwater, M. J., & Shioya, Y., 2003, *MNRAS*, 344, 399
- Bergond, G., Zepf, S. E., Romanowsky, A. J., Sharples, R. M., & Rhode, K. L. 2006, *A&A*, 448, 155
- Bertin, G., & Varri, A. L. 2008, *ApJ*, 689, 1005
- Beers, T. C., Flynn, K., & Gebhardt, K. 1990, *AJ*, 100, 1
- Blakeslee, J. P., & Barber DeGraff, R., 2008, *AJ*, 136, 2295
- Blakeslee, J. P., Jordán, A., Mei, S. et al. 2009, *ApJ*, 694, 556
- Bruns, R. C., Kroupa, P., Fellhauer, M., Metz, M., & Assmann, P., 2011, *A&A*, 529, 138
- Binggeli, B., & Cameron, L. M., 1991, *A&A*, 252, 27
- Binggeli, B., Popescu, C. C., & Tamman, G. A. 1993, *A&AS*, 98, 275
- Binney, J., & Tremaine, S. 2008, *Galactic Dynamics* (2nd ed.; Princeton, NJ: Princeton Univ. Press)
- Brodie, J. P., & Strader, J. 2006, *ARA&A*, 44, 193
- Brodie, J. P., Romanowsky, A. J., Strader, J., & Forbes, D. A. 2011, *ApJ*, 142, 199
- Boley, A. C., Lake, G., Read, J., & Teyssier, R., 2009, *ApJ*, 706, L192
- Caon, N., Capaccioli, M., & D’Onofrio, M. 1993, *MNRAS*, 265, 1013
- Caso, J. P., Bassino, L. P., Richtler, T., Smith Castelli, A. V., & Faifer, F. R. 2013, *MNRAS*, 430, 1088
- Côté, P., Marzke, R. O., & West, M. J. 1998, *ApJ*, 501, 554
- Côté, P., McLaughlin, D. E., Hanes, D. A., et al. 2001, *ApJ*, 559, 828
- Côté, P., Piatek, S., Ferrarese, L., et al. 2006, *ApJS*, 165, 57
- Cohen, J. G., & Ryzhov, A. 1997, *ApJ*, 486, 230
- Cohen, J. G. 2000, *AJ*, 119, 162
- Coccato, L., Gerhard, O., Arnaboldi, M. et al. 2009, *MNRAS*, 394, 1249
- Ciotti, L. 1991, *A&A*, 249, 99
- Ciotti, L., & Bertin, G. 1999, *A&A*, 352, 447
- Chiboucas, K., Tully, R. B., Marzke, R. O., et al. 2011, *ApJ*, 737, 86
- Chilingarian, I. V., Mieske, S., Hilker, M., & Infante, L. 2011, *MNRAS*, 412, 1627
- Dabringhausen, J., Hilker, M., & Kroupa, P. 2008, *MNRAS*, 386, 864
- Da Rocha, C., Mieske, S., Georgiev, I. Y., Hilker, M., Ziegler, B. L., & Mendes de Oliveira, C. 2011, *A&A*, 525, 86
- Dekel, A., Stoehr, F., & Mamon, G. A. et al. 2005, *Nature*, 437, 707
- Doherty, M., Arnaboldi, M., Das, P., et al. 2009, *A&A*, 502, 771
- Drinkwater, M. J., Jones, J. B., Gregg, M. D., & Philipps, S. 2000a, *PASA*, 17, 227
- Drinkwater, M. J., Gregg, M. D., Couch, W. J., et al. 2004, *PASA*, 21, 375
- Diemand, J., Madau, P., & Moore, B. 2005, *MNRAS*, 364, 367
- Durrell, P. R., Côté, P., & Peng, E. W. et al. 2014, *ApJ*, 794, 103
- Evstigneeva, E. A., Gregg, M. D., Drinkwater, M. J., & Hilker, M. 2007, *AJ*, 133, 1722
- Evstigneeva, E. A., Drinkwater, M. J., Peng, C. Y., et al. 2008, *AJ*, 136, 461
- Emsellem, E., Krajnović, D., & Sarzi, M. 2014, *MNRAS*, 445, 79
- Fabricant, D., Fata, R., Roll, J., et al. 2005, *PASP*, 117, 1411
- Fellhauer, M., & Kroupa, P., 2002, *MNRAS*, 330, 642
- Ferrarese, L., Côté, P., & Cuillandre, J.-C., et al. 2012, *ApJS*, 200, 4
- Ferguson, H. C., & Sandage, A. 1989, *ApJ*, 346, 53
- Forté, J. C., Vega, E. I., & Faifer, F. 2012, *MNRAS*, 421, 635
- Franx, M., Illingworth, G., & de Zeeuw, T., 1991, *ApJ*, 383, 112
- Francis, K. J., Drinkwater, M. J., Chilingarian, I. V., Bolt, A. M. & Firth, P. 2012, *MNRAS*, 425, 325
- Firth, P., Drinkwater, M. J., & Karick, A. M. 2008, *MNRAS*, 389, 1539
- Frank, M. J., Hilker, M., Mieske, S., Baumgardt, H., Grebel, E. K., & Infante, L. 2011, *MNRAS*, 414, 70
- Goerdt, T., Moore, B., Kazantzidis, S. et al. 2008, *MNRAS*, 385, 2136
- Gavazzi, G., Boselli, A., Donati, A., Franzetti, P., & Scodreggio, M. 2003, *A&A*, 400, 451
- Geisler, D., Lee, M. G., & Kim, E. 1996, *AJ*, 111, 1529
- Goodman, J., & Binney, J. J. 1984, *MNRAS*, 207, 511
- Graham, A. W., & Driver, S. P. 2005, *PASA*, 22, 118
- Hanes, D. A., Côté, P., Bridges, T. J., et al. 2001, *ApJ*, 559, 812
- Hau, G. K. T., Spitler, L. R., Forbes, D. A., et al. 2009, *MNRAS*, 394, 97
- Harris, W. E. 1996, *AJ*, 112, 1487
- Harris, W. E. 2009, *ApJ*, 703, 939
- Hoffman, L., Cox, T. J., Dutta, S., & Hernquist, L., 2009, *ApJ*, 705, 920
- Hasegan, M., Jordan, A., Cote, P., et al. 2005, *ApJ*, 627, 203
- Hasegan, I. M. 2007, PhD thesis, Rutgers Univ.
- Hansen, S. H. & Moore, B. 2006, *NewA*, 11, 333
- Hilker, M., Infante, L., & Richtler, T. 1999, *A&AS*, 138, 55
- Huchra, J., & Brodie, J., 1987, *AJ*, 93, 779
- Innanen, K. A., Harris, W. E., & Webbink, R. F. 1983, *AJ*, 88, 338
- Jones, J. B., Drinkwater, M. J., Jurek, R. et al. 2006, *AJ*, 131, 312
- Jerjen, H., Binggeli, B., & Barazza, F. D. 2004, *AJ*, 127, 771
- Janowiecki, S., Mihos, J. C., Harding, P., et al. 2010, *ApJ*, 715, 972
- King, I. R. 1966, *AJ*, 71, 64
- Kleyna, J. T., Geller, M. J., Kenyon, S. J., Kurtz, M. J., & Thorstensen, J. R. 1998, *AJ*, 115, 2359
- Kissler-Patig, M., & Gebhardt, K. 1998, *AJ*, 116, 2237
- Kissler-Patig, M., Jordán, A., & Bastian, N. 2006, *A&A*, 448, 1031
- Küpper, A. H. W., Kroupa, P., Baumgardt, H., & Heggie, D. C., 2010, *MNRAS*, 407, 2241
- Liu, C.-Z., Peng, E. W., & Côté, P. et al. 2015, to be submitted
- Long, R. J., & Mao, S. 2010, *MNRAS*, 405, 301
- Lisker, T., Grebel, E. K., Binggeli, B., & Glatt, K. 2007, *ApJ*, 660, 1186
- Mamon, G. A., & Lokas, E. L. 2005, *MNRAS*, 363, 705
- Mamon, G. A., Biviano, A., & Boué, G. 2013, *MNRAS*, 429, 3079
- Mould, J. R., Oke, J. B., de Zeeuw, P. T., & Nemec, J. M. 1990, *AJ*, 99, 1823
- Moore, B., Diemand, J., Madau, P., Zemp, M., & Stadel, J. *MNRAS*, 2006, 368, 563
- Madrid, J. P., & Donzelli, C. J. 2013, *ApJ*, 770, 158
- Merrifield, M. R. & Kuijken, K. 1998, *MNRAS*, 297, 1292
- Mieske, S., Hilker, M., Misgeld, I., Jordán, A., Infante, L., Kissler-Patig, M. 2009, *A&A*, 498, 705
- Misgeld, I., Mieske, S., Hilker, M., Richtler, T., Georgiev, I. Y., & Schuberth, Y. 2011, *A&A*, 531, 4
- Mieske, S., Hilker, M., & Misgeld, I. 2012, *A&A*, 537, 3
- Maraston, C., Bastian, N., Saglia, R. P., et al. 2004, *A&A*, 416, 467
- Madrid, J. P., Graham, A. W., Harris, W. E., et al. 2010, *ApJ*, 722, 1707
- McLaughlin, D. E., Harris, W. E., & Hanes, D. A. 1994, *ApJ*, 422, 486
- McLaughlin, D. E., & van der Marel, R. P., 2005, *ApJS*, 161, 304
- Mihos, J. C., Harding, P., Feldmeier, J., & Morrison, H. 2005, *ApJ*, 631, 41
- Martin, N. F., de Jong J. T. A., & Rix, Hans-Walter, 2008, *ApJ*, 684, 1075
- Mei, S., Blakeslee, J. P., Côté, P., et al. 2007, *ApJ*, 655, 144
- Murray, N. 2009, *ApJ*, 691, 946
- Muñoz, R. P., Puzia, T. H., Lancon, A., et al. 2014, *ApJS*, 210, 4
- Mieske, S., Hilker, M., Jordan, A., et al. 2008, *A&A*, 487, 921
- Moors, J. J. 1988, *The Statistician*, 37, 25
- Moran, C. C., Teyssier, R., & Lake, G. 2014, *MNRAS*, 442, 2826
- Napolitano, N. R., Romanowsky, A. J., Coccato, L., et al. 2009, *MNRAS*, 393, 329
- Napolitano, N. R., Pota, V., Romanowsky, A. J., et al. 2014, *MNRAS*, 439, 659
- Norris, M. A., & Kannappan, S. J. 2011, *MNRAS*, 414, 739
- Paudel, S., Lisker, T., & Janz, J. 2010, *ApJ*, 724, 64
- Peng, E. W., Jordán, A., Côté, P., et al. 2006, *ApJ*, 639, 95
- Peng, E. W., Jordán, A., Blakeslee, J. P., et al. 2009, *ApJ*, 703, 42
- Peng, E. W. et al. in preparation
- Penny, S. J., Forbes, D. A., Strader, J., Usher, C., Brodie, J. P., & Romanowsky, A. J. 2014, *MNRAS*, 439, 3808
- Pfeffer, J., & Baumgardt, H., 2013, *MNRAS*, 433, 1997
- Phillips, S., Parker, Q. A., Schwartzberg, J. M., & Jones, J. B. 1998, *ApJ*, 493, 59
- Pota, V., Forbes, D. A., Romanowsky, A. J., et al. 2013, *MNRAS*, 428, 389

- Prugniel, P., & Simien, F., 1997, A&A, 321, 111  
 Rejkuba, M., Dubath, P., Minniti, D., & Meylan, G. 2007, A&A, 469, 147  
 Renaud, F., Gieles, M., & Boily, C. M. 2011, MNRAS, 418, 759  
 Renaud, F., Bournaud, F., & Duc, P.-A. 2015, MNRAS, 446, 2038  
 Romanowsky, A. J., Strader, J., Brodie, J. P., et al., 2012, ApJ, 748, 29  
 Sérsic, J. L. 1968, Atlas de Galaxias Australes (Cordoba: Observatorio Astronomico)  
 Seth, A. C., van den Bosch, R., Mieske, S., Baumgardt, H., Brok, M. D. et al. 2014, Nature, 513, 398  
 Schwarzschild, M. 1979, ApJ, 232, 236  
 Schlegel, D. J., Finkbeiner, D. P., & Davis, M. 1998, ApJ, 500, 525  
 Strader, J., Romanowsky, A. J., Brodie, J. P., et al. 2011, ApJS, 197, 33 (S11)  
 Strader, J., Seth, A. C., Forbes, D. A., Fabbiano, G., Romanowsky, A. J. et al. 2013, ApJ, 775, L6  
 Statler, T. S. 1991, AJ, 102, 882  
 Sharp, R., Saunders, W., Smith, G., et al. 2006, Proc. SPIE, 6269, 62690G  
 Schindler, S., Binggeli, B., & Bohringer, H. 1999, A&A, 343, 420  
 Syer, D., & Tremaine, S. 1996, MNRAS, 282, 223  
 Smith, R., Sánchez-Janssen, R., Fellhauer, M. et al. 2013, MNRAS, 429, 1066  
 von Hoerner, S. 1957, ApJ, 125, 451  
 van den Bergh, S. 1986, AJ, 91, 271  
 van den Bergh, S., Morbey, C., & Pazder, J. 1991, ApJ, 375, 594  
 van den Bosch, R. C. E., van de Ven, G., Verolme, E. K., Cappellari, M., & de Zeeuw, P. T. 2008, MNRAS, 385, 647  
 Webb, J. J., Sills, A., & Harris, W. E. 2013, ApJ, 779, 94  
 Westfall, K. B., Majewski, S. R., Ostheimer, J. C., Frinchaboy, P. M., Kunkel, W. E., Patterson, R. J., & Link, R. 2006, AJ, 131, 375  
 Zhu, L., Long, R. J., Mao, S., et al. 2014, ApJ, 792, 59

## APPENDIX

*A Quantile-based Alternative for Kurtosis*

As was detailed in the main text, velocity kurtosis is closely related to the orbital structure of a given tracer population. However, as a fourth moment measure, kurtosis in its standard form is more sensitive to heavy tails than to a sharper peak. A given distribution can be broadly divided into five parts, i.e. the peak, the two shoulders (e.g.  $\mu \pm \sigma$ ), and the two tails. The standard kurtosis measures the peakedness and tailedness of a distribution, which is more or less equivalent to measuring the dispersion (i.e. toward the peak and tails) around the shoulders, in the sense that a higher kurtosis indicates a larger dispersion around the two shoulders. Based on this interpretation, Moors (1988) proposed a robust quantile alternative to the standard kurtosis  $G_2$ :

$$T = \frac{(E_7 - E_5) + (E_3 - E_1)}{E_6 - E_2} - 1.23 \quad (1)$$

where  $E_i$  is the  $i$ -th octile. A normal distribution has  $T = 0$ . Moors (1988) showed that, although there is no simple relation between  $T$  and  $G_2$ ,  $T$  is an increasing function of  $G_2$ .

The  $T$  parameter, which is defined by quantiles, is more sensitive to peakedness than the standard kurtosis. The velocity distribution of our UCDs provides a good example to illustrate this point. UCDs have an obviously sharper peak than a Gaussian distribution, but this feature is only reflected in the high  $T$  value, not in the  $G_2$  measurement.

TABLE 5  
ULTRA-COMPACT DWARFS

ID	R.A. (J2000)	Decl. (J2000)	$v_{\text{los}}$	$u^*$	$g$	$r$	$i$	$z$	$K_s$	$E(B-V)$	$r_{\text{h,NGVS}}$	$r_{\text{h,HST}}$
(1)	(deg)	(deg)	(km s <sup>-1</sup> )	(mag)	(mag)	(mag)	(mag)	(mag)	(mag)	(mag)	(pc)	(pc)
(1)	(2)	(3)	(4)	(5)	(6)	(7)	(8)	(9)	(10)	(11)	(12)	(13)
Old Sample <sup>a</sup>												
H27916	187.71521	12.23610	1299±10	22.10±0.01	21.05±0.00	20.52±0.00	20.38±0.00	20.22±0.01	20.48±0.01	0.024	13.5±0.2	13.7
H30401	187.82795	12.26247	1323±46	22.54±0.01	21.59±0.01	21.06±0.00	20.86±0.01	20.74±0.01	20.94±0.02	0.022	11.3±0.2	10.7
H30772	187.74191	12.26728	1224±9	...	20.75	...	19.84	...	...	0.023	...	9.7
H36612	187.48603	12.32538	1601±3	21.11±0.00	19.99±0.00	19.43±0.00	19.16±0.00	19.06±0.00	19.16±0.00	0.027	17.5±0.3	10.9
H44905	187.73785	12.39440	1563±18	22.99±0.02	21.92±0.01	21.37±0.01	21.14±0.01	21.05±0.01	21.13±0.02	0.023	22.3±1.1	18.5
H55930	187.63929	12.49845	1297±4	20.42±0.00	19.24±0.00	18.68±0.00	18.45±0.00	18.33±0.00	18.41±0.00	0.021	32.9±0.5	35.8
S417	187.75616	12.32351	1860±2	21.00±0.00	19.65±0.00	19.03±0.00	18.70±0.00	18.49±0.00	18.40±0.00	0.023	15.0±0.2	14.7
S477	187.74961	12.30030	1651±62	21.01±0.00	20.06±0.00	19.56±0.00	19.34±0.00	19.22±0.00	19.52±0.01	0.023	23.8±0.5	33.5
S547	187.73910	12.42903	714±2	20.46±0.00	18.87±0.00	18.16±0.00	17.76±0.00	17.48±0.00	17.10±0.00	0.022	20.3±2.5	21.6
S672	187.72804	12.36065	735±106	21.85±0.01	20.83±0.00	20.30±0.00	20.08±0.00	19.96±0.00	20.18±0.01	0.024	19.3±3.0	25.9
S682	187.72775	12.33962	1333±106	22.21±0.01	21.30±0.00	20.81±0.00	20.60±0.01	20.50±0.01	20.82±0.02	0.024	20.2±0.3	23.7
S686	187.72421	12.47187	817±106	21.53±0.00	20.58±0.00	20.05±0.00	19.83±0.00	19.70±0.00	19.97±0.01	0.021	16.3±0.6	21.2
S723	187.72399	12.33940	1398±106	22.68±0.01	21.74±0.00	21.21±0.00	21.01±0.01	20.85±0.01	21.12±0.02	0.024	...	16.9
S731	187.72452	12.28682	1020±9	22.24±0.01	21.10±0.00	20.56±0.00	20.25±0.00	20.13±0.01	20.19±0.01	0.024	20.7±0.4	19.0
S796	187.71563	12.34815	1163±106	21.84±0.01	20.81±0.00	20.28±0.00	20.05±0.00	19.92±0.00	20.18±0.01	0.024	11.8±0.1	15.3
S825	187.71263	12.35542	1142±106	22.60±0.01	21.63±0.00	21.12±0.00	20.91±0.01	20.80±0.01	21.17±0.02	0.024	12.8±1.0	13.3
S887	187.70389	12.36544	1811±106	...	21.19	...	20.33	...	...	0.024	...	9.8
S928	187.69875	12.40845	1284±5	20.81±0.00	19.78±0.00	19.26±0.00	19.02±0.00	18.90±0.00	19.06±0.00	0.023	26.1±0.4	23.0
S999	187.69130	12.41709	1467±5	21.35±0.00	20.30±0.00	19.78±0.00	19.52±0.00	19.40±0.00	19.58±0.00	0.022	20.6±0.6	21.9
S1201	187.67423	12.39478	1211±106	22.16±0.01	21.18±0.00	20.66±0.00	20.42±0.00	20.30±0.01	20.60±0.01	0.023	14.5±0.4	29.9
S1508	187.63087	12.42356	2419±140	22.99±0.02	22.01±0.01	21.49±0.01	21.31±0.01	21.25±0.01	21.53±0.03	0.022	22.2±0.4	42.4
S1629	187.61066	12.34572	1129±7	21.44±0.00	20.38±0.00	19.81±0.00	19.63±0.00	19.51±0.00	19.69±0.01	0.023	18.0±0.3	26.4
S5065	187.70854	12.40248	1578±3	21.32±0.01	20.21±0.00	19.67±0.00	19.40±0.00	19.26±0.00	19.33±0.00	0.023	12.4±0.3	13.6
S6004	187.79259	12.26697	1818±77	22.43±0.01	21.32±0.00	20.87±0.00	20.56±0.01	20.43±0.01	20.63±0.01	0.022	0.6±8.4	40.3
S8005	187.69252	12.40641	1883±5	21.56±0.01	20.51±0.00	19.97±0.00	19.74±0.00	19.61±0.00	19.71±0.01	0.022	28.3±0.8	25.9
S8006	187.69436	12.40616	1079±5	21.61±0.01	20.53±0.00	19.99±0.00	19.73±0.00	19.62±0.00	19.75±0.01	0.023	1.0±7.1	21.2
T15886	188.15205	12.34920	1349±13	23.96±0.03	22.97±0.01	22.55±0.01	22.24±0.02	22.22±0.03	22.35±0.05	0.028	10.1±0.3	11.0
VUCD1	187.53155	12.60861	1223±2	20.28±0.00	19.05±0.00	18.51±0.00	18.21±0.00	18.04±0.00	18.05±0.00	0.022	12.3±0.1	12.1
VUCD2	187.70085	12.58636	919±9	20.29±0.00	19.13±0.00	18.57±0.00	18.31±0.00	18.17±0.00	18.25±0.00	0.021	11.1±0.1	14.1
VUCD4	187.76865	11.94347	916±2	20.30±0.00	19.14±0.00	18.64±0.00	18.34±0.00	18.20±0.00	18.34±0.00	0.028	17.8±1.0	25.1
VUCD5	187.79950	12.68364	1290±2	20.44±0.00	19.01±0.00	18.38±0.00	18.01±0.00	17.82±0.00	17.66±0.00	0.025	19.5±0.4	19.2
VUCD6	187.86816	12.41766	2100±2	20.47±0.00	19.32±0.00	18.76±0.00	18.50±0.00	18.35±0.00	18.45±0.00	0.023	13.1±0.3	18.8
VUCD7	187.97040	12.26641	985±3	19.76±0.00	18.49±0.00	17.92±0.00	17.58±0.00	17.39±0.00	17.38±0.00	0.025	19.6±0.4	100.6
VUCD9	188.06074	12.05149	1323±12	20.66±0.00	19.45±0.00	18.90±0.00	18.57±0.00	18.45±0.00	18.48±0.00	0.029	17.5±0.4	25.4
New Sample												
F6	187.69749	12.55047	1341±5	20.71±0.00	19.46±0.00	18.86±0.00	18.56±0.00	18.40±0.00	18.34±0.00	0.021	17.4±0.2	...
F12	187.76079	12.57058	1190±14	20.78±0.00	19.79±0.00	19.28±0.00	19.05±0.00	18.95±0.00	19.18±0.01	0.021	18.2±0.2	...
F16	188.37279	12.17151	1230±18	21.60±0.00	20.57±0.00	20.05±0.00	19.81±0.00	19.70±0.00	19.91±0.01	0.034	12.2±0.3	...



TABLE 5 — *Continued*

ID	R.A. (J2000)	Decl. (J2000)	$v_{\text{los}}$	$u^*$	$g$	$r$	$i$	$z$	$K_s$	$E(B-V)$	$r_{\text{h,NGVS}}$	$r_{\text{h,HST}}$
(1)	(deg)	(deg)	(km s <sup>-1</sup> )	(mag)	(mag)	(mag)	(mag)	(mag)	(mag)	(mag)	(pc)	(pc)
H18539	187.51687	12.12054	1172±9	20.84±0.00	19.73±0.00	19.20±0.00	18.94±0.00	18.85±0.00	19.05±0.00	0.028	11.1±0.2	...
H20718	187.58181	12.15683	861±9	22.15±0.01	21.08±0.00	20.58±0.00	20.38±0.00	20.29±0.01	20.58±0.01	0.027	11.0±0.2	...
H24581	187.83334	12.19947	1283±9	21.61±0.00	20.48±0.00	19.97±0.00	19.71±0.00	19.59±0.00	19.74±0.00	0.023	11.4±0.2	...
H51655	187.94149	12.45586	1320±25	22.30±0.01	21.34±0.00	20.86±0.00	20.64±0.00	20.52±0.01	20.80±0.02	0.025	12.1±0.3	...
H59533	187.76536	12.53695	693±8	21.04±0.00	20.01±0.00	19.51±0.00	19.27±0.00	19.16±0.00	19.38±0.01	0.020	13.0±0.2	...
H65115	187.48801	12.60081	1491±10	21.27±0.00	20.27±0.00	19.79±0.00	19.54±0.00	19.40±0.00	19.69±0.01	0.022	12.8±0.2	...
S41	187.81801	12.31261	1790±31	22.03±0.01	20.94±0.00	20.41±0.00	20.14±0.00	20.02±0.00	20.14±0.01	0.022	26.2±0.4	...
S323	187.76845	12.38923	1157±106	21.65±0.01	20.67±0.00	20.19±0.00	19.95±0.00	19.83±0.00	20.09±0.01	0.023	33.7±0.6	...
S376	187.75891	12.46381	1215±106	21.59±0.01	20.65±0.00	20.15±0.00	19.92±0.00	19.82±0.00	20.09±0.01	0.021	23.4±0.3	...
S804	187.71277	12.43663	1137±7	20.95±0.00	19.67±0.00	19.07±0.00	18.75±0.00	18.56±0.00	18.50±0.00	0.022	13.5±0.3	...
S991	187.69376	12.33826	1004±75	21.82±0.01	20.79±0.00	20.25±0.00	20.00±0.00	19.86±0.00	19.98±0.01	0.024	15.5±0.3	...
S1044	187.68891	12.34263	2023±75	21.70±0.01	20.68±0.00	20.14±0.00	19.91±0.00	19.78±0.00	19.99±0.01	0.024	24.1±0.4	...
S1301	187.66316	12.35901	1086±106	21.75±0.01	20.72±0.00	20.11±0.00	19.91±0.00	19.74±0.00	19.96±0.01	0.023	13.6±0.4	...
S1449	187.64218	12.37956	1100±106	22.37±0.01	21.33±0.00	20.80±0.00	20.59±0.00	20.46±0.01	20.75±0.01	0.022	17.2±0.3	...
S1504	187.63137	12.43405	858±33	21.26±0.00	20.30±0.00	19.75±0.00	19.57±0.00	19.45±0.00	19.75±0.01	0.022	14.7±0.3	...
S1617	187.61207	12.39196	1407±28	21.06±0.00	19.93±0.00	19.35±0.00	19.13±0.00	18.98±0.00	19.08±0.00	0.022	16.7±0.2	...
S1631	187.60730	12.43919	1368±75	21.52±0.00	20.46±0.00	19.93±0.00	19.71±0.00	19.59±0.00	19.72±0.01	0.022	13.5±0.2	...
S6003	187.79226	12.27445	1818±77	22.30±0.01	21.21±0.00	20.68±0.00	20.40±0.00	20.24±0.01	20.42±0.01	0.022	20.3±0.4	...
S9053	187.70126	12.49469	829±106	22.53±0.01	21.39±0.00	20.89±0.00	20.60±0.00	20.56±0.01	20.92±0.04	0.021	30.2±0.6	...
VUCD8	188.01813	12.34176	1647±3	20.76±0.00	19.64±0.00	19.09±0.00	18.82±0.00	18.71±0.00	18.82±0.00	0.026	12.4±0.3	...
VUCD10	187.62858	12.31157	2305±23	20.86±0.00	19.73±0.00	19.18±0.00	18.94±0.00	18.79±0.00	18.90±0.00	0.023	15.4±0.4	...
M87UCD-1	187.83029	12.37554	1136±21	21.48±0.00	20.34±0.00	19.79±0.00	19.53±0.00	19.41±0.00	19.51±0.00	0.023	28.4±0.3	...
M87UCD-2	187.69858	12.14034	1288±14	20.77±0.00	19.73±0.00	19.25±0.00	19.06±0.00	18.90±0.00	19.18±0.00	0.026	23.6±0.4	...
M87UCD-3	187.58354	11.92186	1404±13	20.44±0.00	19.34±0.00	18.77±0.00	18.54±0.00	18.37±0.00	18.53±0.00	0.030	22.9±0.1	...
M87UCD-4	187.59096	12.40067	1279±11	21.33±0.00	19.93±0.00	19.29±0.00	18.96±0.00	18.75±0.00	18.62±0.00	0.023	11.7±0.4	...
M87UCD-5	187.41829	12.45780	1400±27	21.08±0.00	19.96±0.00	19.42±0.00	19.18±0.00	19.08±0.00	19.30±0.00	0.023	21.0±0.2	...
M87UCD-6	187.51025	12.60938	1514±27	21.34±0.00	20.21±0.00	19.69±0.00	19.42±0.00	19.27±0.00	19.37±0.01	0.022	15.0±0.1	...
M87UCD-7	187.52525	12.66499	1160±12	20.65±0.00	19.48±0.00	18.95±0.00	18.67±0.00	18.51±0.00	18.58±0.00	0.021	17.4±0.1	...
M87UCD-8	187.43858	12.85025	1154±18	21.60±0.00	20.51±0.00	19.99±0.00	19.75±0.00	19.63±0.00	19.70±0.01	0.020	12.1±0.1	...
M87UCD-9	187.59571	12.53021	556±12	20.87±0.00	19.75±0.00	19.22±0.00	18.99±0.00	18.89±0.00	19.06±0.01	0.022	17.9±0.1	...
M87UCD-10	187.50812	12.70747	1178±30	20.82±0.00	19.86±0.00	19.41±0.00	19.17±0.00	19.12±0.00	19.35±0.00	0.022	21.9±0.3	...
M87UCD-11	187.62463	12.63949	845±30	21.42±0.00	20.47±0.00	20.00±0.00	19.79±0.00	19.72±0.00	20.02±0.02	0.021	19.0±0.6	...
M87UCD-12	187.63100	12.86572	1497±10	21.51±0.00	20.13±0.00	19.48±0.00	19.17±0.00	19.01±0.00	18.85±0.00	0.021	12.4±0.5	...
M87UCD-13	187.70533	12.62171	1605±7	21.07±0.00	19.95±0.00	19.38±0.00	19.12±0.00	18.98±0.00	19.01±0.01	0.021	12.8±0.2	...
M87UCD-14	187.76812	13.17849	1347±7	21.64±0.01	20.26±0.00	19.67±0.00	19.31±0.00	19.13±0.00	19.03±0.01	0.025	11.2±0.3	...
M87UCD-15	187.99162	13.25948	1261±12	20.71±0.00	19.66±0.00	19.15±0.00	18.90±0.00	18.83±0.00	19.08±0.01	0.027	40.2±0.4	...
M87UCD-16	187.88208	12.69177	1119±12	20.65±0.00	19.49±0.00	18.89±0.00	18.62±0.00	18.46±0.00	18.62±0.00	0.025	38.1±0.2	...
M87UCD-17	187.89638	12.58316	950±7	21.40±0.00	20.10±0.00	19.47±0.00	19.19±0.00	19.00±0.00	19.04±0.00	0.024	11.9±0.3	...
M87UCD-18	187.85313	12.42384	1780±8	20.85±0.00	19.80±0.00	19.27±0.00	19.04±0.00	18.90±0.00	19.09±0.00	0.022	13.2±0.1	...
M87UCD-19	187.99000	12.82488	1086±15	21.38±0.00	20.31±0.00	19.81±0.00	19.55±0.00	19.48±0.00	19.71±0.01	0.023	18.9±0.2	...
M87UCD-20	187.42217	12.66457	1754±105	21.43±0.00	20.25±0.00	19.73±0.00	19.45±0.00	19.30±0.00	19.42±0.01	0.021	16.7±0.3	...
M87UCD-21	187.90599	12.29465	1484±28	21.59±0.00	20.60±0.00	20.16±0.00	19.86±0.00	19.77±0.00	20.02±0.01	0.023	11.4±0.3	...
M87UCD-22	187.46783	12.62716	905±20	22.09±0.01	20.80±0.00	20.21±0.00	19.92±0.00	19.72±0.00	19.72±0.01	0.021	11.7±0.2	...
M87UCD-23	187.42317	12.74100	1314±23	22.13±0.01	20.95±0.00	20.38±0.00	20.10±0.00	19.95±0.00	20.04±0.01	0.022	11.1±0.2	...
M87UCD-24	187.29442	12.71781	1224±34	22.01±0.01	20.88±0.00	20.32±0.00	20.07±0.00	19.97±0.01	20.01±0.01	0.022	12.3±0.2	...
M87UCD-25	187.91054	11.98996	1264±26	21.88±0.01	20.78±0.00	20.26±0.00	20.01±0.00	19.89±0.00	20.13±0.01	0.029	19.4±0.4	...
M87UCD-26	187.56892	12.26579	2030±18	21.05±0.00	20.04±0.00	19.55±0.00	19.30±0.00	19.17±0.00	19.39±0.00	0.023	17.3±0.3	...
M87UCD-27	188.10566	12.33246	1272±23	21.56±0.00	20.52±0.00	20.01±0.00	19.76±0.00	19.69±0.00	19.89±0.01	0.027	11.7±0.3	...
M87UCD-28	187.52553	12.40982	1870±29	21.78±0.00	20.59±0.00	20.03±0.00	19.74±0.00	19.62±0.00	19.68±0.01	0.026	12.9±0.2	...
M87UCD-29	187.02759	12.41012	599±33	21.97±0.01	20.94±0.00	20.42±0.00	20.21±0.00	20.11±0.01	20.32±0.01	0.028	12.6±0.3	...
M87UCD-30	187.15505	12.47934	1534±28	22.06±0.01	21.01±0.00	20.48±0.00	20.25±0.00	20.14±0.01	20.31±0.02	0.024	12.6±0.3	...
M87UCD-31	187.73054	12.41109	1301±30	22.03±0.01	20.95±0.00	20.40±0.00	20.16±0.00	20.01±0.01	20.08±0.01	0.023	9.7±0.1	10.4
M87UCD-32	187.85521	12.32549	1632±34	21.21±0.00	20.22±0.00	19.73±0.00	19.48±0.00	19.39±0.00	19.65±0.00	0.023	33.2±0.5	...
M87UCD-33	188.06020	12.03307	1833±22	21.81±0.01	20.65±0.00	20.09±0.00	19.79±0.00	19.66±0.00	19.70±0.01	0.029	16.3±0.4	...
M87UCD-34	187.31196	11.89551	905±19	21.25±0.00	20.19±0.00	19.65±0.00	19.40±0.00	19.27±0.00	19.45±0.00	0.027	11.7±0.3	...
M87UCD-35	188.09787	11.96527	1007±16	21.36±0.00	20.19±0.00	19.57±0.00	19.34±0.00	19.19±0.00	19.23±0.00	0.032	11.5±0.3	...
M87UCD-36	187.79709	12.50030	1207±21	22.03±0.01	20.76±0.00	20.18±0.00	19.88±0.00	19.74±0.00	19.79±0.01	0.020	12.1±0.4	...
M87UCD-37	187.54091	12.62679	1324±38	22.15±0.01	21.04±0.00	20.52±0.00	20.26±0.00	20.12±0.01	20.20±0.01	0.022	11.3±0.1	...
M87UCD-38	187.62717	12.67106	1154±18	21.31±0.00	20.07±0.00	19.49±0.00	19.20±0.00	19.09±0.00	19.12±0.01	0.022	22.1±0.3	...
M87UCD-39	188.44296	11.95064	1351±23	22.32±0.01	21.00±0.00	20.38±0.00	20.03±0.00	19.85±0.01	19.77±0.01	0.036	11.2±0.2	...

NOTE. — Col.(1): Object ID; Col.(2): Right ascension in decimal degrees (J2000); Col.(3): Declination in decimal degrees (J2000); Col.(4): Heliocentric radial velocity; Cols.(5–9): MegaCam  $u^*griz$  five-band  $3''$ -aperture (in diameter) AB magnitudes (not corrected for Galactic extinction); Col.(10): WIRCam  $K_s$ -band  $3''$ -aperture (in diameter) AB magnitude (not corrected for Galactic extinction); Col.(11): The Galactic reddening determined by Schlegel et al. (1998); Col.(12): Half-light radius (in units of pc) measured on NGVS images; Col.(13): Half-light radius (in units of pc) measured on HST images.

<sup>a</sup> The UCDs have been compiled by Brodie et al. (2011). In addition,  $g$  and  $i$  band photometry for H30772 and S887 is from Brodie et al. (2011)